



Article

Computer Simulations of EMHD Casson Nanofluid Flow of Blood through an Irregular Stenotic Permeable Artery: Application of Koo-Kleinstreuer-Li Correlations

Rishu Gandhi ¹, Bhupendra Kumar Sharma ¹, Nidhish Kumar Mishra ² and Qasem M. Al-Mdallal ^{3,*}¹ Department of Mathematics, Birla Institute of Technology and Science, Pilani 333031, India² Department of Basic Science, College of Science and Theoretical Studies, Saudi Electronic University, Riyadh 11673, Saudi Arabia³ Department of Mathematical Sciences, College of Science, UAE University, Al-Ain P.O. Box 17551, United Arab Emirates

* Correspondence: q.almdallal@uaeu.ac.ae

Abstract: A novel analysis of the electromagnetohydrodynamic (EMHD) non-Newtonian nanofluid blood flow incorporating CuO and Al₂O₃ nanoparticles through a permeable walled diseased artery having irregular stenosis and an aneurysm is analyzed in this paper. The non-Newtonian behavior of blood flow is addressed by the Casson fluid model. The effective viscosity and thermal conductivity of nanofluids are calculated using the Koo-Kleinstreuer-Li model, which takes into account the Brownian motion of nanoparticles. The mild stenosis approximation is employed to reduce the bi-directional flow of blood to uni-directional. The blood flow is influenced by an electric field along with a magnetic field perpendicular to the blood flow. The governing mathematical equations are solved using Crank-Nicolson finite difference approach. The model has been developed and validated by comparing the current results to previously published benchmarks that are peculiar to this study. The results are utilized to investigate the impact of physical factors on momentum diffusion and heat transfer. The Nusselt number escalates with increasing CuO nanoparticle diameter and diminishing the diameter of Al₂O₃ nanoparticles. The relative % variation in Nusselt number enhances with Magnetic number, whereas a declining trend is obtained for the electric field parameter. The present study's findings may be helpful in the diagnosis of hemodynamic abnormalities and the fields of nano-hemodynamics, nano-pharmacology, drug delivery, tissue regeneration, wound healing, and blood purification systems.

Keywords: KKL correlations; Casson fluid; stenosis and aneurysm; nanoparticles; radiation

Citation: Gandhi, R.; Sharma, B.K.; Mishra, N.K.; Al-Mdallal, Q.M. Computer Simulations of EMHD Casson Nanofluid Flow of Blood through an Irregular Stenotic Permeable Artery: Application of Koo-Kleinstreuer-Li Correlations. *Nanomaterials* **2023**, *13*, 652. <https://doi.org/10.3390/nano13040652>

Academic Editor: Manuel M. Piñeiro

Received: 24 December 2022

Revised: 14 January 2023

Accepted: 16 January 2023

Published: 7 February 2023



Copyright: © 2023 by the authors. Licensee MDPI, Basel, Switzerland. This article is an open access article distributed under the terms and conditions of the Creative Commons Attribution (CC BY) license (<https://creativecommons.org/licenses/by/4.0/>).

1. Introduction

The World Health Organization (WHO) reports that 68 percent of deaths are caused by non-communicable diseases, of which cardiovascular disorders account for one-third. According to evidence from various physiological studies, disorders of the blood arteries and the heart, such as heart attacks and strokes, are the major cause of mortality globally. Atherosclerosis, a condition that results in plaque building up in the artery lumen and manifesting as stenosis, causes these events because it prevents blood from reaching distant body cells. An aneurysm may be caused by multiple factors that result in the breaking down of the well-organized structural components (proteins) of the aortic wall that provide support and stabilize the wall. The exact cause has yet to be fully discovered. Atherosclerosis is thought to play an essential role in aneurysmal disease. Numerous researchers ([1–7]) have theoretically and experimentally explored the mechanics of blood circulation via stenosed arteries. The physical characteristics of EMHD of the bloodstream through an artery in the presence of electroosmotic forces with both aneurysm and stenosis are theoretically investigated by Abdesalam et al. [8]. Zhang et al. [9] studied the impacts

of nanoparticle volume fraction on plaque disintegration during transit by employing a two-phase mixing approach. By assuming that blood viscosity is hematocrit-dependent, Poonam et al. [10] analyzed the impact of hybrid nanoparticles on hemodynamical blood flow parameters via a curved artery with aneurysm and stenosis. Basha et al. [11] examined the fluid transport behavior of Au-Cu/Blood hybrid nanofluid via an artery having the inclination and irregular stenosis. Using computational fluid dynamics (CFD) in COMSOL Multiphysics, Waqas et al. [12] investigated the numerical modeling of hybrid nanofluid with nanoparticles such as gold and silver over a stenotic artery.

A novel class of functional fluids known as "nanofluids" has been produced by the colloidal combination of these nanoparticles in the conventional base fluid, having less effective thermophysical properties. As a result, the nanofluid generated has increased thermal conductivity, thermal diffusivity, viscosity, and convective heat transfer coefficient, among other thermophysical properties. These nanoparticles, or nanofluids, have been used strategically in numerous heat transfer applications with outstanding success. However, more biomedical engineering applications, such as drug transport, tissue regeneration, wound healing, and biomagnetic nano-pharmacodynamics, are beginning to emerge. Badfar et al. [13] used Fe_3O_4 nanoparticles coated with a drug to carry out the magnetic drug targeting in the vessel's stenosis region. They also investigated how the wire's location as a magnetic source affected the MDT. In their numerical simulation of magnetic nanoparticle-based medication delivery, Varmazyar et al. [14] used two cases: one with a slight obstruction and the other with two mild and severe blockages. Ramadan et al. [15] analyzed the blood flow incorporating gold nanoparticles via a stenosed tapering artery using the Phan-Thien-Tanner fluid model to treat the terrible cancer disease. In order to accurately characterize the blood flow, including TiO_2 and Ag nanoparticles, Saeed et al. [16] used a couple-stress fluid model. Sharma et al. [17] carried out entropy analysis for blood flow with temperature-dependent viscosity through a tapered artery having multiple-stenosis incorporating hybrid nanoparticles. Mekheimer et al. [18] used biomedical models of drug distribution via nanoparticles to address the issue of synovitis in sick tissues. Khanduri et al. [19] investigated the influence of Hall and ion slips on MHD blood flow through a catheterized artery with multiple stenosis and thrombosis while suspending Au and GO nanoparticles in the blood. Sharma et al. [20] analyzed the effects of heat transfer and body acceleration on unsteady MHD blood flow through a curved artery in the presence of stenosis and aneurysm using hybrid nanoparticles. Dolui et al. [21] investigated the combined influence of non-linear thermal radiation and externally induced magnetic field to graphically evaluate the flow characteristics of tri-hybrid (Cu-Ag-Au), hybrid (Cu-Au), and single (Au) nanofluids flowing through arteries with composite stenosis. Karmakar et al. [22] formulated a mathematical framework for the hemodynamical characterization of blood circulation containing trihybrid nanoparticles inside an eccentric endoscopic artery canal with a flexible wall in the presence of buoyancy and electro-osmotic pressures.

The majority of the research described above treated blood as a Newtonian fluid and investigated the relationship between arterial stenosis and blood flow dynamics. The blood behaves in the larger-diameter arteries with an assertive Newtonian behavior when shear rates are greater than 100 s^{-1} . However, because blood is a suspension of cells, it is widely known that arteries with smaller diameters and lower shear rates exhibit remarkable non-Newtonian blood behavior. The Casson fluid flow model has recently become more well-known attributable to its intriguing applications in everyday life. The Casson fluid flow model is widely used in modern science. Casson fluid exhibits yield stress characteristics. The Casson fluid changes into the Newtonian fluid when the yield stress is high enough. Walawender et al. [23] showed that blood can be modeled using Casson fluid by measuring pressure drop and volumetric flow rate experimentally. Sarifuddin et al. [24] used the Marker and Cell approach to numerically solve the equations as they investigated the effect of two-dimensional blood flow while supposing blood to be Casson fluid flowing through an unsteady stenosed artery. Using the Casson model to describe the

liquid's non-Newtonian viscosity, Debnath et al. [25] investigated the effects of a 1st-order homogeneous-heterogeneous chemical reaction in an annular pipe. Darcy's law was applied by Ali et al. [26] to examine the Casson fluid flow behavior in a 2-D porous channel using a vorticity-stream function method. Das et al. [27] explored solute dispersion via a stenotic tube with an absorptive wall in their study with Casson fluid characterizing the rheology of blood. Padma et al. [28] aimed to investigate how yield stress affected the EMHD motion of Casson fluid and nanoparticles as they flow via a mildly blocked inclined tapering artery.

In their study of blood flow through stenosed arteries, most researchers assumed the artery walls to be impermeable. The primary function of an endothelial wall in the human body is to prevent the exchange of substances between moving tissues and blood. In actuality, the endothelium wall is permeable due to the presence of ultramicroporous structures. Increased permeability is caused by the accumulation of cholesterol, fatty acids, dilated artery walls, and arterial wall injury. Beaver and Joseph's [29] experimental work revealed that Darcy's law would not always satisfy the governing equations near the wall. So, they also formulated a boundary condition at the permeable wall. Mishra et al. [30] analyzed the influence of the wall's permeability via an artery having composite stenosis. Ijaz and Nadeem [31] discussed how the blood flows through a permeable walled stenosed artery is affected by copper nanoparticles. Akbar et al. [32] formulated a mathematical model to simulate blood flow through a composite stenosed artery with permeable walls. Shahzadi and Bilal [33] investigated the flow of blood in a stenosed bifurcated artery containing Copper and its oxide as a drug to reduce the stress and lesions of an atherosclerotic artery. They considered the artery to be permeable as well as compliant. A mathematical model for medication delivery employing gold and alumina nanoparticles via a porous artery with stenosis was developed by Gandhi et al. [34]. In their computational analysis through a curved stenosed permeable artery, Sharma et al. [35] took into account the blood flow in two phases - the core and the plasma region, respectively. Further, Kumawat et al. [36] examined the entropy generation with a chemical reaction through a permeable curved artery. Sharma and Gandhi [37] investigated unsteady heat and mass transmission through a stretching surface immersed in a Darcy-Forchheimer porous medium.

None previously mentioned research assessed the KKL model for the effective thermal conductivity and viscosity models. The primary focus of engineers, physicians, and biologists is on improving the working fluid's thermal performance. The nanosized particle dispersion in the base fluid is one of the current methods. Now, it is a well-known truth that nanoparticles of one sort or more are trustworthy agents for improving the thermal performance of the working fluid. There are several documented relationships between the thermal characteristics of the base fluid, nanofluid, and solid nanoparticles. One set of relationships has more restrictions than another, though. The role of nanoparticles in drug delivery mechanisms is the most effective technique to cure several problems such as atherosclerosis, aneurysms, angina, or heart attacks. Also, the main concern of physicians during any surgery is to regulate the human body temperature in the presence of external factors such as radiation, heat source, etc. The literature survey reveals that the KKL correlations ([38–40]) take temperature, volume fraction, and nanoparticle size into account when calculating how Brownian motion would affect a fluid's thermal performance. To replicate the nanofluid flow between two parallel plates—one of which is heated from the outside and the other into which coolant fluid is injected, Kandelousi [41] used KKL correlations. Mehmood et al. [42] used the KKL model to assess the effective thermal conductivity and dynamic viscosity of the alumina-water nanofluid in a porous cavity under the influence of an inclined magnetic field. By combining the Cattaneo-Christov flux model with KKL correlations and considering the dispersion of CuO and Al₂O₃ nanoparticles in blood, Rana and Nawaz [43] examined the improvement of heat transmission. Utilizing the KKL model, Malik et al. [44] thoroughly examined fluid flow between two vertical rotating plates with permeable surfaces, including nanoparticles. Shahzad et al. [45] investigated the behavior of Sutterby nanofluid passing through a sloping sheet considering copper oxide-engine oil

(CuO-EO). They determined the effective viscosity and thermal conductivity using the KKL model. Ramzan et al. [46] investigated the heat transmission of MHD water-based nano liquid flow across a permeable stretched curved surface affected by an induced magnetic field by employing KKL correlations for dynamic viscosity and thermal conductivity.

The literature survey shows that no work has been published yet that addresses optimizing heat transfer utilizing the Casson fluid model and KKL correlations along with temperature-dependent viscosity through the irregular stenotic artery with an aneurysm. Therefore, the present study aims to study the blood flow through a stenotic artery with an aneurysm affected by the magnetic field, electric field, Joule heating, radiation, and viscous dissipation. The present work is divided into five main sections: The first part is the introduction concerning KKL correlations and other parameters considered in this work. Secondly, we have the mathematical modeling part, which initially describes KKL correlations for the simulation of nanofluid. Afterward, the model’s geometrical representation and governing equations are presented, followed by non-dimensionalization and radial coordinate transformation. The third section deals with the numerical solution, which firstly discusses the discretization of governing equations and then the validation of the employed Crank-Nicolson finite difference scheme. The validation of the present work is divided into two parts: (i) mesh independence and (ii) validation with existing literature. The following section is the results and graphical analysis, which discusses the influence of various influential parameters involved in the flow. The novelty of the present work is expressed as:

- KKL correlations are employed for modeling nanofluid flow through a permeable stenosed artery.
- EMHD Casson fluid flow is considered along with Joule heating, radiation, and viscous dissipation.
- The relative % variation for the Nusselt number has been calculated and portrayed using bar graphs.

2. Mathematical Formulation

An unsteady, incompressible, laminar, viscous, electrically conducting EMHD blood flow through a permeable artery with irregular stenosis and aneurysm is under consideration. A cylindrical coordinate system $(r_1^*, \tilde{\theta}, z_1^*)$ is employed with r_1^* and z_1^* as radial and axial directions, respectively. The axial symmetry of the artery corresponds to the independence of flow in the azimuthal ($\tilde{\theta}$) direction. The blood behavior is assumed non-Newtonian and is represented using Casson fluid model. The KKL-correlations are used to address variable thermal conductivity and viscosity. A uniform magnetic field B_0 along with an electric field E_0 is applied perpendicular to the axial direction (z_1^* -direction) of blood flow. The magnetic Reynold’s number is assumed to be very small ($Re_M \ll 1$); therefore, the induced magnetic field is neglected compared to the applied magnetic field.

2.1. Mathematical Representation of the Stenosis and Aneurysm

The geometry of the stenosis and aneurysm is assumed as ([47,48]):

$$R(z_1^*) = \begin{cases} R_0 - 2\delta \left[\cos\left(\frac{2\pi}{L_0} \left(\frac{z_1^* - d}{2} - \frac{L_0}{4}\right)\right) - \frac{7}{100} \cos\left(\frac{32\pi}{L_0} \left(z_1^* - d - \frac{L_0}{2}\right)\right) \right], & d \leq z_1^* \leq d + L_0, \\ R_0 + 2\delta \left[\cos\left(\frac{2\pi}{L_0} \left(\frac{z_1^* - d}{2} - \frac{L_0}{4}\right)\right) - \frac{7}{100} \cos\left(\frac{32\pi}{L_0} \left(z_1^* - d - \frac{L_0}{2}\right)\right) \right], & d + 2L_0 \leq z_1^* \leq d + 3L_0, \\ R_0, & \text{otherwise.} \end{cases} \tag{1}$$

2.2. Governing Equations

The velocity and temperature fields are represented as:

$$\tilde{V}^* = \tilde{V}^*[u_1^*(r_1^*, z_1^*, t_1^*), 0, w_1^*(r_1^*, z_1^*, t_1^*)], \quad \tilde{T}^* = \tilde{T}^*(r_1^*, z_1^*, t_1^*)$$

due to the bidirectional flow of blood through a stenosed artery with aneurysm (Figure 1).

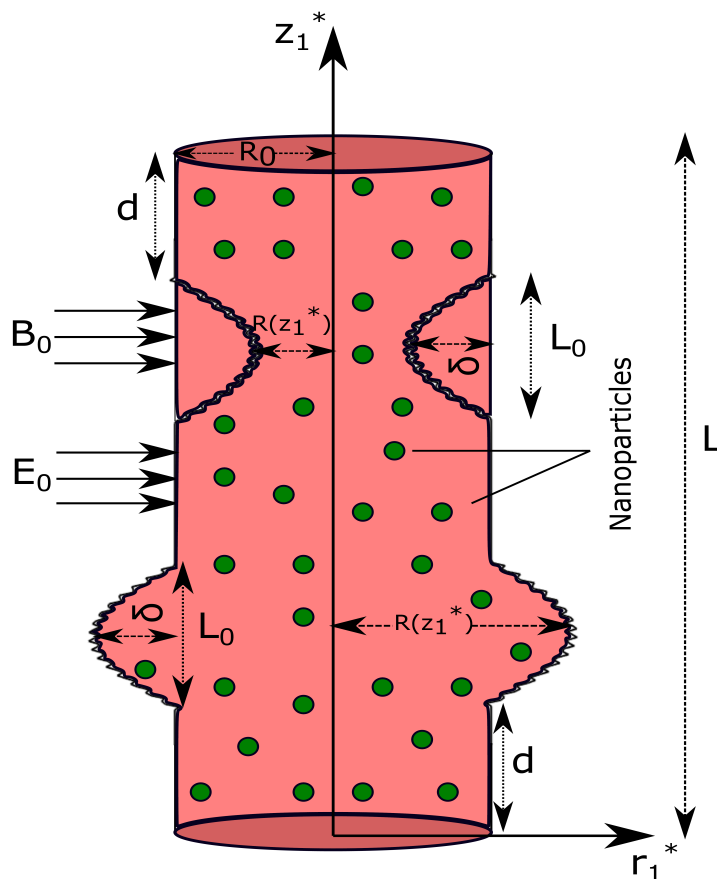


Figure 1. Physical sketch of artery with time variant stenosis and aneurysm.

Under the above assumptions and invoking the Boussinesq approximation, the governing equations for the flow are represented as ([34,48]):

Continuity Equation:

$$\frac{1}{r_1^*} \frac{\partial(r_1^* u_1^*)}{\partial r_1^*} + \frac{\partial w_1^*}{\partial z_1^*} = 0, \tag{2}$$

Momentum Equation:

r_1^* -direction:

$$\rho_{nf} \left[\frac{D u_1^*}{D t} \right] = -\frac{\partial p_1^*}{\partial r_1^*} + \frac{1}{r_1^*} \frac{\partial}{\partial r_1^*} (r_1^* \tau_{r_1^* r_1^*}) + \frac{\partial \tau_{z_1^* r_1^*}}{\partial z_1^*} - \frac{\tau_{\theta \theta}}{r_1^*}, \tag{3}$$

z_1^* -direction:

$$\rho_{nf} \left[\frac{D w_1^*}{D t} \right] = -\frac{\partial p_1^*}{\partial z_1^*} + \frac{1}{r_1^*} \frac{\partial}{\partial r_1^*} (r_1^* \tau_{r_1^* z_1^*}) + \frac{\partial \tau_{z_1^* z_1^*}}{\partial z_1^*} + (\rho \gamma)_{nf} g (\tilde{T}^* - \tilde{T}_1^*) - \sigma_{nf} (B_0^2 w_1^* - E_0 B_0), \tag{4}$$

Energy Equation:

$$(\rho C_p)_{nf} \left[\frac{\partial \tilde{T}^*}{\partial t_1^*} + u_1^* \frac{\partial \tilde{T}^*}{\partial r_1^*} + w_1^* \frac{\partial \tilde{T}^*}{\partial z_1^*} \right] = k_{eff} \left[\frac{1}{r_1^*} \frac{\partial}{\partial r_1^*} \left(r_1^* \frac{\partial \tilde{T}^*}{\partial r_1^*} \right) + \frac{\partial^2 \tilde{T}^*}{\partial z_1^{*2}} \right] - \frac{\partial q_r^*}{\partial r_1^*} + \sigma_{nf} (B_0 w_1^* - E_0 B_0)^2 + \phi^* \tag{5}$$

The Casson fluid model’s rheological equation of state for an incompressible flow is as follows ([26]):

$$\tau_{ij}^* = \begin{cases} 2 \left(\mu_b^* + \frac{p_y^*}{\sqrt{2\pi_c^*}} \right) e_{ij}^*, & \pi^* > \pi_c^* \\ 2 \left(\mu_b^* + \frac{p_y^*}{\sqrt{2\pi_c^*}} \right) e_{ij}^*, & \pi^* \leq \pi_c^* \end{cases} \tag{6}$$

where $\pi^* = e_{ij}^* \cdot e_{ij}^*$ is the product of deformation rate with itself, π_c^* is a critical value based on the non-Newtonian model, μ_b^* is the plastic dynamic viscosity of the non-Newtonian fluid, and p_y^* is the yield stress of the fluid.

When $\pi^* \leq \pi_c^*$, Equation (6) can be expressed as:

$$\tau_{ij}^* = 2\mu_b^* \left(1 + \frac{1}{\beta} \right) e_{ij}^* \tag{7}$$

where $\beta = \frac{\mu_b^* \sqrt{2\pi_c^*}}{p_y^*}$ is the Casson fluid parameter.

On incorporating the Casson fluid properties mentioned in Equation (7), the governing Equations (2)–(5) become:

Continuity Equation:

$$\frac{\partial u_1^*}{\partial r_1^*} + \frac{u_1^*}{r_1^*} + \frac{\partial w_1^*}{\partial z_1^*} = 0, \tag{8}$$

Momentum Equation:

r_1^* -direction:

$$\rho_{nf} \left[\frac{\partial u_1^*}{\partial t_1^*} + u_1^* \frac{\partial u_1^*}{\partial r_1^*} + w_1^* \frac{\partial u_1^*}{\partial z_1^*} \right] = -\frac{\partial p_1^*}{\partial r_1^*} + \frac{1}{r_1^*} \frac{\partial}{\partial r_1^*} \left[\mu_{eff} \left(1 + \frac{1}{\beta} \right) r_1^* \frac{\partial u_1^*}{\partial r_1^*} \right] + \frac{1}{2} \frac{\partial}{\partial z_1^*} \left[\mu_{eff} \left(1 + \frac{1}{\beta} \right) \left(\frac{\partial w_1^*}{\partial r_1^*} + \frac{\partial u_1^*}{\partial z_1^*} \right) \right] - \mu_{eff} \left(1 + \frac{1}{\beta} \right) \frac{u_1^*}{r_1^{*2}}, \tag{9}$$

z_1^* -direction:

$$\rho_{nf} \left[\frac{\partial w_1^*}{\partial t_1^*} + u_1^* \frac{\partial w_1^*}{\partial r_1^*} + w_1^* \frac{\partial w_1^*}{\partial z_1^*} \right] = -\frac{\partial p_1^*}{\partial z_1^*} + \frac{1}{2} \frac{1}{r_1^*} \frac{\partial}{\partial r_1^*} \left[\mu_{eff} \left(1 + \frac{1}{\beta} \right) r_1^* \left(\frac{\partial u_1^*}{\partial z_1^*} + \frac{\partial w_1^*}{\partial r_1^*} \right) \right] + \frac{\partial}{\partial z_1^*} \left[\mu_{eff} \left(1 + \frac{1}{\beta} \right) \frac{\partial w_1^*}{\partial z_1^*} \right] + (\rho\gamma)_{nf} g (\tilde{T}^* - \tilde{T}_1^*) - \sigma_{nf} (B_0^2 w_1^* - E_0 B_0), \tag{10}$$

Energy Equation:

$$(\rho C_p)_{nf} \left[\frac{\partial \tilde{T}^*}{\partial t_1^*} + u_1^* \frac{\partial \tilde{T}^*}{\partial r_1^*} + w_1^* \frac{\partial \tilde{T}^*}{\partial z_1^*} \right] = k_{eff} \left[\frac{1}{r_1^*} \frac{\partial}{\partial r_1^*} \left(r_1^* \frac{\partial \tilde{T}^*}{\partial r_1^*} \right) + \frac{\partial^2 \tilde{T}^*}{\partial z_1^{*2}} \right] - \frac{\partial q_r^*}{\partial r_1^*} + \sigma_{nf} (B_0 w_1^* - E_0 B_0)^2 + \phi^*, \tag{11}$$

where

$$q_r^* = -\frac{4\sigma_e}{3k_e} \frac{\partial \tilde{T}^4}{\partial r_1^*}, \tag{12}$$

and

$$\phi^* = 2\mu_{eff} \left(1 + \frac{1}{\beta}\right) \left[\left(\frac{\partial u_1^*}{\partial r_1^*}\right)^2 + \left(\frac{u_1^*}{r_1^*}\right)^2 + \left(\frac{\partial w_1^*}{\partial z_1^*}\right)^2 + \frac{1}{2} \left(\frac{\partial u_1^*}{\partial z_1^*} + \frac{\partial w_1^*}{\partial r_1^*}\right)^2 \right]. \quad (13)$$

It is assumed that there are minimal temperature changes within the blood flow. Therefore, \tilde{T}^4 in Equation (12) is linearized by disregarding higher-order terms and is expanded using Taylor series around \tilde{T}_1^* :

$$\tilde{T}^{*4} = 4\tilde{T}_1^{*3}\tilde{T} - 3\tilde{T}_1^{*4},$$

Hence, Equation (12) becomes

$$q_r^* = -\frac{16\tilde{T}_1^{*3}\sigma_e}{3k_e k_f} \frac{\partial \tilde{T}}{\partial r_1^*}.$$

The boundary conditions are ([31,48]):

$$\frac{\partial w_1^*}{\partial r_1^*} = 0, \frac{\partial \tilde{T}^*}{\partial r_1^*} = 0 \text{ at } r_1^* = 0, \quad (14)$$

$$w_1^* = w_s, \frac{\partial w_1^*}{\partial r_1^*} = \frac{\alpha}{\sqrt{k_1^*}}(w_s - w_{porous}), \tilde{T}^* = \tilde{T}_w^* \text{ at } r_1^* = R, \quad (15)$$

where w_{porous} is the velocity in the permeable boundary, k_1^* is the permeability of the medium, α is the slip parameter that is dimensionless and characterizes the structure of the permeable material within the boundary region depending on the material parameters.

The initial conditions of the flow are assumed as:

$$w_1^*|_{t_1^*=0} = 0, \tilde{T}^*|_{t_1^*=0} = 0. \quad (16)$$

2.3. Koo-Kleinstreuer-Li (KKL) Correlation for Nanofluid Simulation

The fluid's thermal conductivity is strongly influenced by Brownian motion. In order to account for effective thermal conductivity, Koo and Kleinstreuer [38] assumed that it consists of two parts: the general static part given by Maxwell correlation and the other is the Brownian motion part. The implications of particle size, particle volume fraction, temperature dependency, and combinations of base fluid and particles are all taken into account by this thermal conductivity model.

$$k_{eff} = k_{st} + k_{Br}, \quad (17)$$

$$\frac{k_{st}}{k_f} = 1 + \frac{3\left(\frac{k_p}{k_f} - 1\right)\phi}{\left(\frac{k_p}{k_f} + 2\right) - \left(\frac{k_p}{k_f} - 1\right)\phi}, \quad (18)$$

Koo [39] inserted two empirical functions (β_1 and \tilde{f}) to incorporate the interaction among nanoparticles and the temperature influence in the model, resulting in:

$$k_{Br} = 5 \times 10^4 \beta_1 \phi (\rho C_p)_f \sqrt{\frac{\kappa_b T}{\rho_p d_p}} \tilde{f}(\phi, T). \quad (19)$$

The significance of the interfacial thermal resistance acting among base fluids and nanoparticles has been increasingly emphasized in recent years. The thin layer acting as a barrier is crucial in reducing the effective thermal conductivity of the nanoparticle, and it is

thought that the thermal interfacial resistance (also known as Kapitza resistance) exists in the neighboring layers of the two distinct materials.

Li [40] reexamined the approach used by Koo and Kleinstreuer [49] and integrated the function \tilde{f} and β_1 to create a new function \tilde{F} that accounts for the particle volume fraction, diameter, and temperature. The empirical function \tilde{F} depends on the type of nanofluid [40]. Additionally, a new $k_{p,eff}$ has been introduced and therefore k_p in Equation (18) is replaced by $k_{p,eff}$ which is given by:

$$R_f + \frac{d_p}{k_p} = \frac{d_p}{k_{p,eff}}, \quad (20)$$

where R_f is interfacial thermal resistance and has value $4 \times 10^{-8} \text{ km}^2/\text{W}$.

For CuO-Blood and Al_2O_3 -Blood nanofluids, \tilde{F} is defined as follows ([43]):

$$\begin{aligned} \tilde{F}(\phi, T, d_p) = & (b_1 + b_2 \ln(d_p) + b_3 \ln(\phi) + b_4 \ln(\phi) \ln(d_p) + b_5 \ln(d_p)^2) \ln(T) \\ & + (b_6 + b_7 \ln(d_p) + b_8 \ln(\phi) + b_9 \ln(\phi) \ln(d_p) + b_{10} \ln(d_p)^2), \\ & \phi \leq 0.04, 300\text{K} \leq T \leq 325\text{K} \quad (21) \end{aligned}$$

with the coefficients b_i ($i = 1 \dots 10$) are based on the type of nanoparticles used in the analysis.

The Koo-Kleinstreuer-Li (KKL) correlation is finally written as ([49]):

$$k_{Br} = 5 \times 10^4 \phi \tilde{F}(\phi, T, d_p) (\rho C_p)_f \sqrt{\frac{\kappa_b T}{\rho_p d_p}}. \quad (22)$$

The effective viscosity of the nanofluid is given as ([49]):

$$\mu_{eff} = \mu_{st} + \mu_{Br} = \mu_{st} + \frac{k_{Br}}{k_f} \times \frac{\mu_f}{Pr}, \quad (23)$$

where,

$$\mu_{st} = \frac{\mu_f}{(1 - \phi_1)^{2.5}}.$$

Here, the Reynold's viscosity model [50] is considered to address the fluid's viscosity μ_f given by:

$$\mu_f(\tilde{\theta}) = \mu_0 e^{-\beta_0 \tilde{\theta}} = \mu_0 [1 - \beta_0 \tilde{\theta}] \quad \text{where } \beta_0 \ll 1. \quad (24)$$

Therefore,

$$\begin{aligned} \mu_{eff} &= \frac{\mu_0 (1 - \beta_0 \tilde{\theta})}{(1 - \phi_1)^{2.5}} + \frac{k_{Br}}{k_f} \times \frac{\mu_0 (1 - \beta_0 \tilde{\theta})}{Pr} \\ \mu_{eff} &= \mu_0 (1 - \beta_0 \tilde{\theta}) \left(\frac{1}{(1 - \phi_1)^{2.5}} + \frac{k_{Br}}{k_f Pr} \right). \quad (25) \end{aligned}$$

Thermophysical Features of Nanofluid

The density (ρ_{nf}), heat capacity ($(\rho C_p)_{nf}$), electrical conductivity (σ_{nf}) and thermal expansion coefficient (γ_{nf}) of nanofluid are given by the usual relations as follows ([34,51]):

$$\rho_{nf} = (1 - \phi) \rho_f + \phi \rho_p \quad (26)$$

$$(\rho C_p)_{nf} = (1 - \phi) (\rho C_p)_f + \phi (\rho C_p)_p \quad (27)$$

$$\sigma_{nf} = \sigma_f \left(1 + \frac{3(\sigma - 1)\phi}{(\sigma + 2) - (\sigma - 1)\phi} \right), \quad \sigma = \frac{\sigma_p}{\sigma_f}. \quad (28)$$

$$\gamma_{nf} = (1 - \phi)(\gamma)_f + \phi_1(\gamma)_p \tag{29}$$

2.4. Nanoparticle and Base Fluid Features

Table 1 lists the thermophysical characteristics of the blood and nanoparticles utilized in the study, and Table 2 provides the coefficient values of copper oxide and aluminum oxide.

Table 1. Thermophysical properties of nanoparticles ([43]).

Thermophysical Properties	Blood	CuO	Al ₂ O ₃
Density [$\rho(\text{kg/m}^3)$]	1060	6500	3970
Thermal Conductivity [$K(\text{W/mK})$]	0.492	18	25
Electrical Conductivity [$\sigma(\text{S/m})$]	0.667	1×10^{-10}	3.5×10^7
Thermal Expansion Coefficient [$\gamma \times 10^{-5}(\text{K}^{-1})$]	0.18	0.5	0.85
Heat Capacitance [$C_p(\text{J/kgK})$]	3770	540	765
d_p	–	47	29

Table 2. The coefficient values of CuO and Al₂O₃ nanoparticles ([43]).

Coefficient	CuO	Al ₂ O ₃
b_1	–26.593310846	52.813488759
b_2	–0.403818333	6.115637295
b_3	–33.3516805	1 0.6955745084
b_4	–1.915825591	$4.1745552786 \times 10^{-2}$
b_5	$6.42185846658 \times 10^{-2}$	0.176919300241
b_6	48.40336955	–298.19819084
b_7	–9.787756683	–34.532716906
b_8	190.245610009	–3.9225289283
b_9	10.9285386565	–0.2354329626
b_{10}	–0.72009983664	–0.999063481

2.5. Non-Dimensional Analysis

The governing equations given by (8)–(11) need to be transformed into dimensionless form so that a numerical solution is obtained. The non-dimensional variables are introduced as:

$$\begin{aligned} \bar{r}_1^* &= \frac{r_1^*}{R_0}, \bar{w}_1^* = \frac{w_1^*}{U_0}, \bar{u}_1^* = \frac{L_0 u_1^*}{\delta^* U_0}, \bar{t}_1^* = \frac{U_0 t_1^*}{R_0}, \bar{z}_1^* = \frac{z_1^*}{L_0}, \bar{p}_1^* = \frac{R_0^2 p_1^*}{U_0 L_0 \mu_f}, \bar{\theta} = \frac{\tilde{T}^* - \tilde{T}_1^*}{\tilde{T}_w^* - \tilde{T}_1^*}, \bar{R} = \frac{R}{R_0}, \\ \alpha &= \frac{\alpha^* L_0}{R_0}, \bar{d} = \frac{d}{L_0}, \bar{w}_s = \frac{w_s}{U_0}, Re = \frac{U_0 \rho_f R_0}{\mu_f}, M^2 = \frac{\sigma_f B_0^2 R_0^2}{\mu_f}, Gr = \frac{\rho_f R_0^2 g \gamma_f (\tilde{T}_w^* - \tilde{T}_1^*)}{\mu_f U_0}, \\ Ec &= \frac{U_0^2}{C_p (\tilde{T}_w^* - \tilde{T}_1^*)}, Pr = \frac{\mu_f C_p}{k_f}, Nr = \frac{16 \sigma_e \tilde{T}_1^{*3}}{3 k_f k_e}. \end{aligned} \tag{30}$$

The insertion of the above non-dimensional parameters mentioned in (18), disregarding the bars and using the mild stenotic hypotheses that the maximal stenosis height is less than the artery’s radius, i.e., $\delta (= \delta^*/R_0) \ll 1$, and the artery’s radius and the stenotic region’s length are proportionate, i.e., $\epsilon (= R_0/L_0) = O(1)$ leads to the modified form of governing Equations (8)–(11), which are as follows:

Continuity Equation:

$$\frac{\partial w_1^*}{\partial z_1^*} = 0, \tag{31}$$

Momentum Equation:

r-direction:

$$\frac{\partial p_1^*}{\partial r_1^*} = 0, \tag{32}$$

z-direction:

$$Re \frac{\rho_{nf}}{\rho_f} \frac{\partial w_1^*}{\partial t_1^*} = -\frac{\partial p_1^*}{\partial z_1^*} + \frac{1}{2r_1^*} \frac{\partial}{\partial r_1^*} \left[\frac{\mu_{eff}}{\mu_0} \left(1 + \frac{1}{\beta} \right) r_1^* \frac{\partial w_1^*}{\partial r_1^*} \right] + \frac{(\rho\gamma)_{nf}}{(\rho\gamma)_f} Gr\tilde{\theta} - \frac{\sigma_{nf}}{\sigma_f} M^2 (w_1^* - E_1^*), \tag{33}$$

Energy Equation:

$$\frac{(\rho C_p)_{nf}}{(\rho C_p)_f} \frac{\partial \tilde{\theta}}{\partial t_1^*} = \frac{1}{RePr} \frac{k_{eff}}{k_f} \left[\frac{\partial^2 \tilde{\theta}}{\partial r_1^{*2}} + \frac{1}{r_1^*} \frac{\partial \tilde{\theta}}{\partial r_1^*} \right] + \frac{Nr}{RePr} \frac{\partial^2 \tilde{\theta}}{\partial r_1^{*2}} + \frac{\sigma_{nf}}{\sigma_f} \frac{EcM^2}{Re} (w_1^* - E_1^*)^2 + \frac{\mu_{eff}}{\mu_0} \left(1 + \frac{1}{\beta} \right) \frac{Ec}{Re} \left[\left(\frac{\partial w_1^*}{\partial r_1^*} \right)^2 \right]. \tag{34}$$

The geometry of stenosis, aneurysm and boundary conditions in the dimensionless form can be described as ([48]):

$$R(z_1^*) = \begin{cases} \left[1 - 2\delta^* \left[\cos \left(2\pi \left(\frac{z_1^* - d}{2} - \frac{1}{4} \right) \right) - \frac{7}{100} \cos \left(32\pi \left(z_1^* - d - \frac{1}{2} \right) \right) \right] \right], & d \leq z_1^* \leq d + 1, \\ \left[1 + 2\delta^* \left[\cos \left(2\pi \left(\frac{z_1^* - d}{2} - \frac{1}{4} \right) \right) - \frac{7}{100} \cos \left(32\pi \left(z_1^* - d - \frac{1}{2} \right) \right) \right] \right], & d + 2 \leq z_1^* \leq d + 3, \\ 1, & \text{otherwise.} \end{cases} \tag{35}$$

$$\frac{\partial w_1^*}{\partial r_1^*} \Big|_{r_1^*=0} = 0, w_1^*(r_1^*, t_1^*) \Big|_{r_1^*=R} = w_s, \frac{\partial w_1^*}{\partial r_1^*} \Big|_{r_1^*=R} = \frac{\alpha}{\sqrt{Da}} (w_s - w_{porous}), \tag{36}$$

where

$$w_{porous} = -\frac{Da}{\mu_{nf}} \frac{dp}{dz}.$$

Blood flows through the cardiovascular system due to the heart’s pumping motion, causing a pressure gradient across the vascular network. The pressure gradient is separated into two parts: non-fluctuating (continuous) and fluctuating (pulsatile) [52] as given below:

$$-\frac{\partial p_1^*}{\partial z_1^*} = A_0 + A_1 \cos(w_p t_1^*), t_1^* > 0, \tag{37}$$

where, A_0 and A_1 signify the amplitudes of the steady-state and pulsatile pressure gradient components, respectively, and $w_p = 2\pi f_p$, f_p depicts the heart pulse frequency.

On the substitution of dimensionless variables in (37), the modified equation for the pressure gradient becomes:

$$-\frac{\partial p_1^*}{\partial z_1^*} = B_1 [1 + e \cos(c_1 t_1^*)], \tag{38}$$

where

$$e = \frac{A_1}{A_0}, B_1 = \frac{A_0 R_0^2}{\mu_0 U_0}, c_1 = \frac{2\pi R_0 f_p}{U_0}. \tag{39}$$

Using Equation (38) in Equation (33), we have:

$$Re \frac{\rho_{nf}}{\rho_f} \frac{\partial w_1^*}{\partial t_1^*} = B_1 [1 + e \cos(c_1 t_1^*)] + \frac{1}{2r_1^*} \left(1 + \frac{1}{\beta} \right) \left(\frac{1}{(1 - \phi_1)^{2.5}} + \frac{k_{Br}}{k_f Pr} \right) \frac{\partial}{\partial r_1^*} \left[(1 - \beta_0 \tilde{\theta}) r_1^* \frac{\partial w_1^*}{\partial r_1^*} \right] + \frac{(\rho\gamma)_{nf}}{(\rho\gamma)_f} Gr\tilde{\theta} - \frac{\sigma_{nf}}{\sigma_f} M^2 (w_1^* - E_1^*). \tag{40}$$

2.6. Radial Coordinate Transformation

The physical geometry taken into account in the formulated problem is cylindrical, i.e., a cylindrical coordinate system is considered. However, in order to use the computational approach, the considered geometry needs to be transformed into a rectangular domain by employing the transformation $(x_1^* = \frac{r_1^*}{R(z_1^*)})$. On applying this transformation, the Equations (40) and (34) become:

$$Re \frac{\rho_{nf}}{\rho_f} \frac{\partial w_1^*}{\partial t_1^*} = B_1 [1 + e \cos(c_1 t_1^*)] + \frac{1}{2R^2} \left(1 + \frac{1}{\beta}\right) \left(\frac{1}{(1 - \phi_1)^{2.5}} + \frac{k_{Br}}{k_f Pr}\right) \times \left[(1 - \beta_0 \tilde{\theta}) \left(\frac{\partial^2 w_1^*}{\partial x_1^{*2}} + \frac{1}{x_1^*} \frac{\partial w_1^*}{\partial x_1^*}\right) - \beta_0 \frac{\partial \tilde{\theta}}{\partial x_1^*} \frac{\partial w_1^*}{\partial x_1^*} \right] + \frac{(\rho\gamma)_{nf}}{(\rho\gamma)_f} Gr \tilde{\theta} - \frac{\sigma_{nf}}{\sigma_f} M^2 (w_1^* - E_1^*), \quad (41)$$

$$\frac{(\rho C_p)_{nf}}{(\rho C_p)_f} \frac{\partial \tilde{\theta}}{\partial t_1^*} = \frac{1}{Re Pr} \frac{k_{eff}}{k_f} \left(\frac{1}{R^2}\right) \left[\frac{\partial^2 \tilde{\theta}}{\partial x_1^{*2}} + \frac{1}{x_1^*} \frac{\partial \tilde{\theta}}{\partial x_1^*}\right] + \left(\frac{1}{R^2}\right) \frac{Nr}{Re Pr} \frac{\partial^2 \tilde{\theta}}{\partial x_1^{*2}} + \frac{\sigma_{nf}}{\sigma_f} \frac{Ec M^2}{Re} (w_1^* - E_1^*)^2 + \frac{1}{R^2} \left(1 + \frac{1}{\beta}\right) \left(\frac{Ec}{Re}\right) (1 - \beta_0 \tilde{\theta}) \left(\frac{1}{(1 - \phi_1)^{2.5}} + \frac{k_{Br}}{k_f Pr}\right) \left(\frac{\partial w_1^*}{\partial x_1^*}\right)^2. \quad (42)$$

The wall shear stress (WSS), volumetric flow rate, and resistance impedance are expressed as:

$$\tau_w = -\frac{1}{R} \left(\frac{\partial w_1^*}{\partial x_1^*}\right)_{x_1^*=1}, \quad (43)$$

$$Q_1 = 2\pi R^2 \int_0^1 w_1^* x_1^* dx_1^*, \quad (44)$$

$$\lambda = \frac{L \left(\frac{\partial p_1^*}{\partial z_1^*}\right)}{Q_1}. \quad (45)$$

3. Numerical Procedure

The partial differential Equations (41) and (42) are coupled differential equations, therefore obtaining an analytic solution is too difficult. On the other hand, numerical approaches can yield a highly accurate solution. An unconditionally stable implicit finite difference (Crank–Nicolson) approach is used in this case. The superscripts and subscripts are not taken into account throughout the discretization process for Equations (41) and (42).

3.1. Discretization

On employing the values of thermophysical features of nanofluid and discretizing the governing Equations (41) and (42) using Crank-Nicolson scheme, the desired form of equations is:

$$\begin{aligned}
 \left[(1 - \phi) + \phi \frac{\rho_p}{\rho_f} \right] Re \left[\frac{w_i^{k+1} - w_i^k}{dt} \right] &= B_1 [1 + e \cos(c_1 t^k)] + \frac{1}{2} \left(1 + \frac{1}{\beta} \right) \left(\frac{1}{R^2} \right) (1 - \beta_0 \tilde{\theta}_i^k) \\
 &\times \left(\frac{1}{(1 - \phi_1)^{2.5}} + \frac{k_{Brownian}}{k_f Pr} \right) \times \left[\frac{1}{2} \left(\frac{w_{i+1}^{k+1} - 2w_i^{k+1} + w_{i-1}^{k+1}}{dx^2} + \frac{w_{i+1}^k - 2w_i^k + w_{i-1}^k}{dx^2} \right) \right. \\
 &+ \frac{1}{2x(i)} \left(\frac{w_{i+1}^{k+1} - w_{i-1}^{k+1}}{2dx} + \frac{w_{i+1}^k - w_{i-1}^k}{2dx} \right) \left. - \frac{\beta_0}{2R^2} \left(1 + \frac{1}{\beta} \right) \left(\frac{1}{(1 - \phi_1)^{2.5}} + \frac{k_{Br}}{k_f Pr} \right) \right. \\
 &\times \left[\left(\frac{\tilde{\theta}_{i+1}^{k+1} - \tilde{\theta}_{i-1}^{k+1}}{4dx} + \frac{\tilde{\theta}_{i+1}^k - \tilde{\theta}_{i-1}^k}{4dx} \right) \left(\frac{w_{i+1}^{k+1} - w_{i-1}^{k+1}}{4dx} + \frac{w_{i+1}^k - w_{i-1}^k}{4dx} \right) \right] \\
 &+ \left[(1 - \phi) + \phi \frac{(\rho\gamma)_p}{(\rho\gamma)_f} \right] Gr \tilde{\theta}_i^k - \frac{1}{2} \frac{\sigma_{nf}}{\sigma_f} M^2 (w_i^k + w_i^{k+1}) + \frac{\sigma_{nf}}{\sigma_f} M^2 E_1^*, \quad (46)
 \end{aligned}$$

$$\begin{aligned}
 \left[(1 - \phi) + \phi \frac{(\rho C_p)_p}{(\rho C_p)_f} \right] \left[\frac{\tilde{\theta}_i^{k+1} - \tilde{\theta}_i^k}{dt} \right] &= \frac{1}{Re Pr} \frac{k_{nf}}{k_f} \left(\frac{1}{R^2} \right) \left[\frac{1}{2} \left(\frac{\tilde{\theta}_{i+1}^{k+1} - 2\tilde{\theta}_i^{k+1} + \tilde{\theta}_{i-1}^{k+1}}{dx^2} \right. \right. \\
 &+ \left. \left. \frac{\tilde{\theta}_{i+1}^k - 2\tilde{\theta}_i^k + \tilde{\theta}_{i-1}^k}{dx^2} \right) + \frac{1}{2x(i)} \left(\frac{\tilde{\theta}_{i+1}^{k+1} - \tilde{\theta}_{i-1}^{k+1}}{2dx} + \frac{\tilde{\theta}_{i+1}^k - \tilde{\theta}_{i-1}^k}{2dx} \right) \right] \\
 &+ \left(\frac{1}{2R^2} \right) \frac{Nr}{Re Pr} \left(\frac{\tilde{\theta}_{i+1}^{k+1} - 2\tilde{\theta}_i^{k+1} + \tilde{\theta}_{i-1}^{k+1}}{dx^2} + \frac{\tilde{\theta}_{i+1}^k - 2\tilde{\theta}_i^k + \tilde{\theta}_{i-1}^k}{dx^2} \right) + \left(1 + \frac{1}{\beta} \right) \left(\frac{1}{R^2} \right) \\
 &\times \left(1 - \frac{\beta_0}{2} (\tilde{\theta}_i^{k+1} + \tilde{\theta}_i^k) \right) \left(\frac{1}{(1 - \phi_1)^{2.5}} + \frac{k_{Br}}{k_f Pr} \right) \left[\frac{1}{2} \left(\frac{w_{i+1}^{k+1} - w_{i-1}^{k+1}}{2dx} + \frac{w_{i+1}^k - w_{i-1}^k}{2dx} \right) \right]^2 \\
 &+ \frac{\sigma_{nf}}{\sigma_f} \frac{Ec M^2}{Re} \left[\frac{1}{2} (w_i^{k+1} + w_i^k) - E_1^* \right]^2. \quad (47)
 \end{aligned}$$

The Crank-Nicolson scheme employed in the current analysis is, however, stable for all values for dt and dx still, a minimal value is considered with great precision as $dt = 10^{-4}$ and $dx = 10^{-4}$. It is noticed that no further change occurs in the values of hemodynamical parameters studied in the research with decreasing values of dt and dx . A total of $N + 1$ grid points have been considered in the spatial direction, with $x = 1/(N + 1)$ being the step size, whereas $M + 1$ grid points are considered temporal. The value at any time instant t^k is given as $t^k = (k - 1)dt$, dt being a small increment in time. As the scheme employed is an implicit one; therefore a system of equations is obtained, and it is in the form of a tri-diagonal system which can be solved with the Tri-diagonal Matrix Algorithm (TDMA) [53].

Equation (46) corresponds to a tri-diagonal system, which is given by

$$A_i^k w_{i-1}^{k+1} + B_i^k w_i^{k+1} + C_i^k w_{i+1}^{k+1} = A_i^k w_{i-1}^k + B_i^k w_i^k + C_i^k w_{i+1}^k + D_i^k, \quad (48)$$

where

$$\begin{aligned}
 A_i^k &= - \left(1 + \frac{1}{\beta} \right) \left(\frac{(1 - \beta_0 \tilde{\theta}_i^k)}{(1 - \phi)^{2.5}} + \frac{k_{Br}}{k_f Pr} \right) \left(\frac{1}{4R^2} \right) \left(\frac{dt}{dx^2} - \frac{1}{2x(i)} \frac{dt}{dx} \right) - \frac{\beta_0}{8R^2} \left(\frac{dt}{dx} \right) \left(1 + \frac{1}{\beta} \right) \left(\frac{1}{(1 - \phi_1)^{2.5}} + \frac{k_{Br}}{k_f Pr} \right) \times \left(\frac{\tilde{\theta}_{i+1}^{k+1} - \tilde{\theta}_{i-1}^{k+1}}{2dx} + \frac{\tilde{\theta}_{i+1}^k - \tilde{\theta}_{i-1}^k}{2dx} \right), \\
 B_i^k &= Re \left[(1 - \phi) + \phi \frac{\rho_p}{\rho_f} \right] + \left(\frac{1}{2R^2} \right) \left(\frac{dt}{dx^2} \right) \left(1 + \frac{1}{\beta} \right) \left(\frac{(1 - \beta_0 \tilde{\theta}_i^k)}{(1 - \phi)^{2.5}} + \frac{k_{Br}}{k_f Pr} \right) + \frac{dt}{2} \frac{\sigma_{nf}}{\sigma_f} M^2, \\
 C_i^k &= - \left(1 + \frac{1}{\beta} \right) \left(\frac{(1 - \beta_0 \tilde{\theta}_i^k)}{(1 - \phi)^{2.5}} + \frac{k_{Br}}{k_f Pr} \right) \left(\frac{1}{4R^2} \right) \left(\frac{dt}{dx^2} + \frac{1}{2x(i)} \frac{dt}{dx} \right) + \frac{\beta_0}{8R^2} \left(\frac{dt}{dx} \right) \left(1 + \frac{1}{\beta} \right) \left(\frac{1}{(1 - \phi_1)^{2.5}} + \frac{k_{Br}}{k_f Pr} \right) \times \left(\frac{\tilde{\theta}_{i+1}^{k+1} - \tilde{\theta}_{i-1}^{k+1}}{2dx} + \frac{\tilde{\theta}_{i+1}^k - \tilde{\theta}_{i-1}^k}{2dx} \right),
 \end{aligned}$$

$$\begin{aligned}
 A_i^k &= \left(1 + \frac{1}{\beta}\right) \left(\frac{(1-\beta_0\tilde{\theta}_i^k)}{(1-\phi)^{2.5}} + \frac{k_{Br}}{k_f Pr}\right) \left(\frac{1}{4R^2}\right) \left(\frac{dt}{dx^2} - \frac{1}{2x(i)} \frac{dt}{dx}\right) + \frac{\beta_0}{8R^2} \left(\frac{dt}{dx}\right) \left(1 + \frac{1}{\beta}\right) \left(\frac{1}{(1-\phi_1)^{2.5}} + \frac{k_{Br}}{k_f Pr}\right) \times \left(\frac{\tilde{\theta}_{i+1}^{k+1} - \tilde{\theta}_{i-1}^{k+1}}{2dx} + \frac{\tilde{\theta}_{i+1}^k - \tilde{\theta}_{i-1}^k}{2dx}\right), \\
 B_i^k &= Re \left[(1-\phi) + \phi \frac{\rho_p}{\rho_f} \right] - \left(\frac{1}{2R^2}\right) \left(\frac{dt}{dx^2}\right) \left(1 + \frac{1}{\beta}\right) \left(\frac{(1-\beta_0\tilde{\theta}_i^k)}{(1-\phi)^{2.5}} + \frac{k_{Br}}{k_f Pr}\right) - \frac{dt}{2} \frac{\sigma_{nf}}{\sigma_f} M^2, \\
 C_i^k &= \left(1 + \frac{1}{\beta}\right) \left(\frac{(1-\beta_0\tilde{\theta}_i^k)}{(1-\phi)^{2.5}} + \frac{k_{Br}}{k_f Pr}\right) \left(\frac{1}{4R^2}\right) \left(\frac{dt}{dx^2} + \frac{1}{2x(i)} \frac{dt}{dx}\right) - \frac{\beta_0}{8R^2} \left(\frac{dt}{dx}\right) \left(1 + \frac{1}{\beta}\right) \left(\frac{1}{(1-\phi_1)^{2.5}} + \frac{k_{Br}}{k_f Pr}\right) \times \left(\frac{\tilde{\theta}_{i+1}^{k+1} - \tilde{\theta}_{i-1}^{k+1}}{2dx} + \frac{\tilde{\theta}_{i+1}^k - \tilde{\theta}_{i-1}^k}{2dx}\right), \\
 D_i^k &= dt B_1 [1 + ecos(c_1 t^k)] + dt \left[(1-\phi) + \phi \frac{(\rho\gamma)_p}{(\rho\gamma)_f} \right] Gr \tilde{\theta}_i^k + dt \frac{\sigma_{nf}}{\sigma_f} M^2 E_1^*.
 \end{aligned}$$

The tri-diagonal system corresponding to Equation (47) is given by

$$P_i^k \theta_{i-1}^{k+1} + Q_i^k \theta_i^{k+1} + S_i^k \theta_{i+1}^{k+1} = P_i^k \theta_{i-1}^k + Q_i^k \theta_i^k + S_i^k \theta_{i+1}^k + F_i^k, \tag{49}$$

where

$$\begin{aligned}
 P_i^k &= -\frac{1}{RePr} \left(\frac{1}{2R^2}\right) \left[\frac{k_{nf}}{k_f} \left(\frac{dt}{dx^2} - \frac{1}{2x(i)} \frac{dt}{dx}\right) + Nr \frac{dt}{dx^2} \right], \\
 Q_i^k &= \left[(1-\phi) + \phi \frac{(\rho C_p)_p}{(\rho C_p)_f} \right] + \frac{1}{RePr} \frac{1}{R^2} \frac{dt}{dx^2} \left(\frac{k_{nf}}{k_f} + Nr\right) + dt \frac{\beta_0}{(1-\phi)^{2.5}} \left(1 + \frac{1}{\beta}\right) \frac{Ec}{Re} \left(\frac{1}{2R^2}\right) \\
 &\times \left[\frac{1}{2} \left(\frac{w_{i+1}^{k+1} - w_{i-1}^{k+1}}{2dx} + \frac{w_{i+1}^k - w_{i-1}^k}{2dx}\right) \right]^2, \\
 S_i^k &= -\frac{1}{RePr} \left(\frac{1}{2R^2}\right) \left[\frac{k_{nf}}{k_f} \left(\frac{dt}{dx^2} + \frac{1}{2x(i)} \frac{dt}{dx}\right) + Nr \frac{dt}{dx^2} \right], \\
 P_i^k &= \frac{1}{RePr} \left(\frac{1}{2R^2}\right) \left[\frac{k_{nf}}{k_f} \left(\frac{dt}{dx^2} - \frac{1}{2x(i)} \frac{dt}{dx}\right) + Nr \frac{dt}{dx^2} \right], \\
 Q_i^k &= \left[(1-\phi) + \phi \frac{(\rho C_p)_p}{(\rho C_p)_f} \right] - \frac{1}{RePr} \frac{1}{R^2} \frac{dt}{dx^2} \left(\frac{k_{nf}}{k_f} + Nr\right) - dt \frac{\beta_0}{(1-\phi)^{2.5}} \left(1 + \frac{1}{\beta}\right) \frac{Ec}{Re} \left(\frac{1}{2R^2}\right) \\
 &\times \left[\frac{1}{2} \left(\frac{w_{i+1}^{k+1} - w_{i-1}^{k+1}}{2dx} + \frac{w_{i+1}^k - w_{i-1}^k}{2dx}\right) \right]^2, \\
 S_i^k &= \frac{1}{RePr} \left(\frac{1}{2R^2}\right) \left[\frac{k_{nf}}{k_f} \left(\frac{dt}{dx^2} + \frac{1}{2x(i)} \frac{dt}{dx}\right) + Nr \frac{dt}{dx^2} \right]. \\
 F_i^k &= dt \frac{\sigma_{nf}}{\sigma_f} \frac{EcM^2}{Re} \left[\frac{1}{2} \left(w_i^{k+1} + w_i^k\right) - E_1^* \right]^2 + dt \left(1 + \frac{1}{\beta}\right) \left(\frac{1}{(1-\phi)^{2.5}} + \frac{k_{Brownian}}{k_f Pr_f}\right) \frac{Ec}{Re} \left(\frac{1}{R^2}\right) \\
 &\times \left[\frac{1}{2} \left(\frac{w_{i+1}^{k+1} - w_{i-1}^{k+1}}{2dx} + \frac{w_{i+1}^k - w_{i-1}^k}{2dx}\right) \right]^2.
 \end{aligned}$$

3.2. Validation of the Employed Numerical Scheme

The Crank-Nicolson finite difference method has been applied in the present work. To check the accuracy of the applied numerical scheme, two methods have been adopted. Firstly, a mesh independence test is performed, which includes both grid independence as well as time independence. Also, validation has been performed with the existing model of Zaman et al. [54].

3.2.1. Mesh Independence

A “grid-independency test” is used to optimize the suggested grid system for the current study, allowing for the selection of a mesh density that is both computationally accurate and economically acceptable. Table 3 lists the ideal grid size (100 × 100) that achieves enough precision; any other mesh size refinement does not provide an increase in accuracy. In accordance with Table 4, the “time-independency test” provides the best time-step size of dt = 0.01.

Table 3. Grid Independence.

Grid Size	Wall Shear Stress (τ_w)
25 × 25	0.0082
50 × 50	0.0035
70 × 70	0.0022
100 × 100	0.0018
200 × 200	0.0018

Table 4. Time Independence.

Time Step Size (dt)	Wall Shear Stress (τ_w)
0.1	0.0035
0.08	0.0038
0.05	0.0042
0.02	0.0045
0.01	0.0044

3.2.2. Validation with Existing Literature

The accuracy of our results has been verified by validating it with the existing model of Zaman et al. [54]. The effect of EMHD, Joule heating, viscous dissipation, and radiation has been neglected to verify the results with the simplest existing model of Zaman et al. [54]. As the Casson fluid parameter in the current work approaches infinity ($\beta \rightarrow \infty$), the current model approaches the Newtonian model in [54]. The KKL scheme adopted for variable viscosity and thermal conductivity is also replaced by a generalized model for nanofluids. The results have been compared for Al_2O_3 nanoparticles, which are common in both research work. For verification, Figure 2a,b have been plotted. A comparison with the existing literature [54] reveals a good agreement to support the validity of the present solutions.

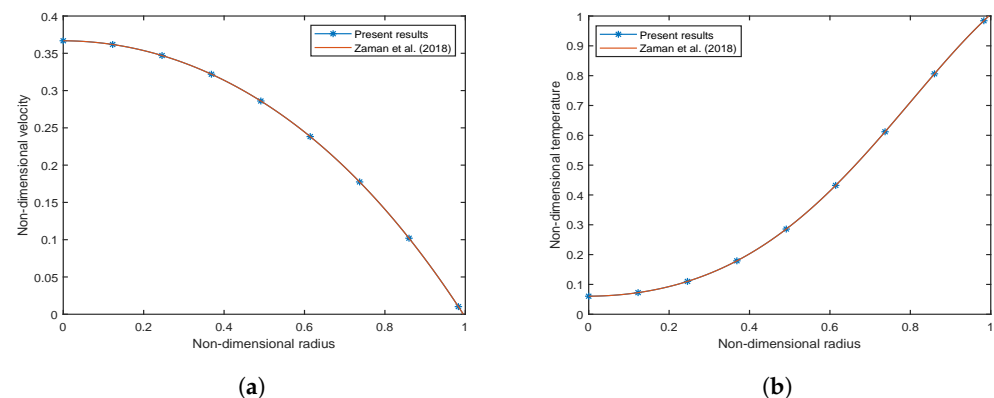


Figure 2. Comparison results (a) non-dimensional velocity for $Gr = 0.5$, (b) non-dimensional temperature for $\phi_2 = 0.01$.

4. Results and Graphical Analysis

In this section, the impact of various flow parameters such as electric field parameter (E_1^*), viscosity parameter (β_0), volume fractions of both the nanoparticles (ϕ_1, ϕ_2), Casson fluid parameter (β), radiation parameter (Nr), Eckert number (Ec), and Prandtl number (Pr) on non-dimensional velocity, wall shear stress, flow rate, non-dimensional temperature, and Nusselt number is analyzed. A comparison of CuO -Blood and Al_2O_3 -Blood nanofluid has been conducted. The default values of the emerging parameters are mentioned in Table 5, and the range of non-dimensional parameters considered in the present analysis are depicted in Table 6.

Table 5. Default Values of emerging parameters ([48]).

Parameters	ϕ_1	ϕ_2	d	B_1	c_1	e	δ	β_0	w_s	β	α
Value	0.03	0.03	0.56	1.41	1	0.2	0.1	0.5	0.1	2	0.1

Table 6. Range of influential flow parameters.

Flow Parameter	Range	References
Magnetic Field Parameter (M^2)	0–5	[37]
Casson fluid Parameter (β)	1–10	[29]
Grashof number (Gr)	0–0.5	[34,36]
Eckert number (Ec)	0–1	[36]
Prandtl number (Pr)	14–25	[46]
Radiation Parameter (Nr)	0–2	[18,25]

4.1. Nusselt Number and Enhancement Ratio

The ratio of thermal energy conducted in the fluid to thermal energy undertaken in the fluid is expressed by the Nusselt number. It represents the convective heat transfer taking place at the surface and is equivalent to the dimensionless temperature gradient at the surface. Therefore, the Nusselt number is mathematically represented as:

$$Nu = \sqrt{Re} \frac{k_{eff}}{k_f} (1 + Nr) \frac{1}{R} \left(\frac{\partial \tilde{\theta}}{\partial x_1^*} \right)_{x_1^*=1}. \quad (50)$$

The temperature plays a vital role during any treatment or surgery; therefore, regulating it is the primary concern of physicians. The two types of nanoparticles are considered in the present study, namely CuO and Al₂O₃ nanoparticles. They both have opposing effects on the temperature profile. Therefore, a relative % variation has been performed to decide which nanoparticle will be suitable in the required situation and is given by:

$$\text{Relative \% Variation} = \frac{Nu(Al_2O_3) - Nu(CuO)}{Nu(Al_2O_3)} \times 100 \quad (51)$$

Figures 3–5 show relative % error for various influential parameters, namely Magnetic number M^2 , electric field parameter E_1^* , Eckert number Ec, radiation parameter Nr, Casson fluid parameter β , and Prandtl number Pr. Figure 3a depicts that a decreasing trend in Nusselt number is analyzed with increasing values of M^2 whereas the relative % variation show enhancement as M^2 varies from 1 to 5. The Nusselt number and relative % variation decline with increasing E_1^* values as shown in Figure 3b. Figure 4 illustrates that relative % variation declines with rising Eckert number values. In contrast, an opposite trend is analyzed with proliferating radiation parameter values, i.e., relative % variation booms with mounting Nr values. The Nusselt number inclines whereas relative % variation declines with enlarging β values as indicated by Figure 5a. Figure 5b exhibits an increase in Nusselt number and relative % variation with ascending values of Prandtl number.

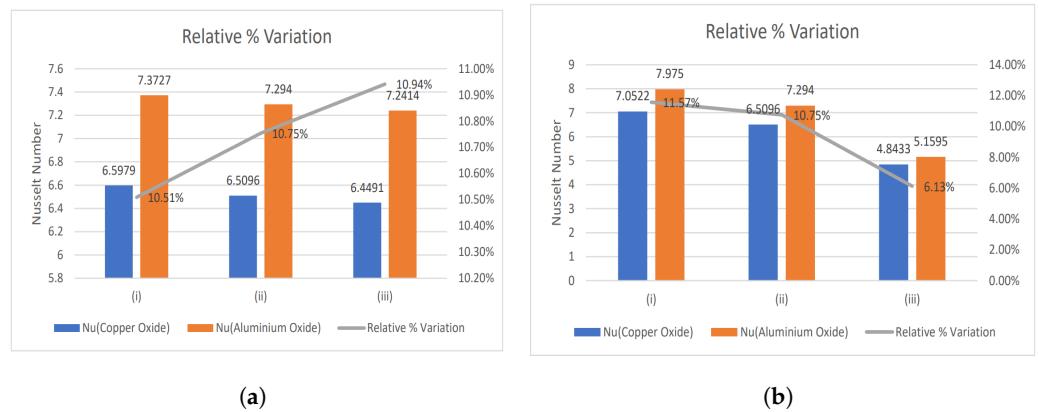


Figure 3. Relative % variation for (a) Magnetic number (i) $M^2 = 1$, (ii) $M^2 = 3$, (iii) $M^2 = 5$, and (b) Electric field parameter (i) $E_1^* = 0.1$, (ii) $E_1^* = 0.3$, (iii) $E_1^* = 0.6$.

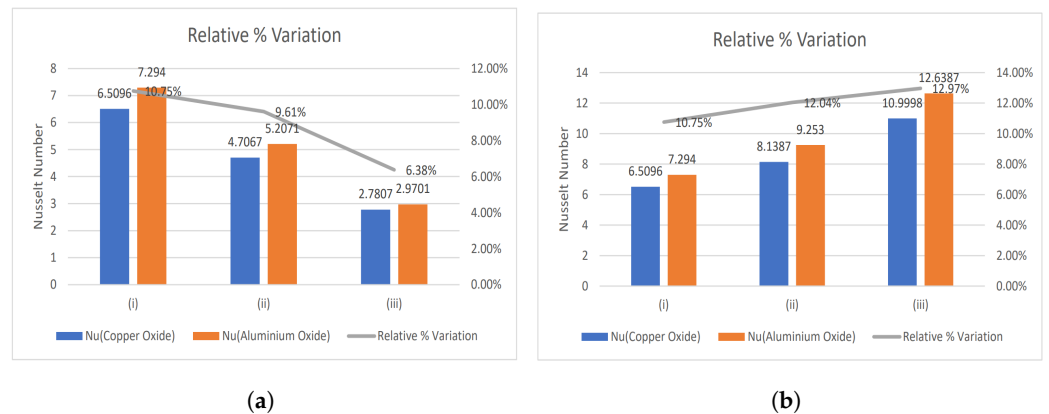


Figure 4. Relative % variation for (a) Eckert number (i) $Ec = 0.2$, (ii) $Ec = 0.4$, (iii) $Ec = 0.6$, and (b) Radiation parameter (i) $Nr = 0.5$, (ii) $Nr = 1$, (iii) $Nr = 2$.

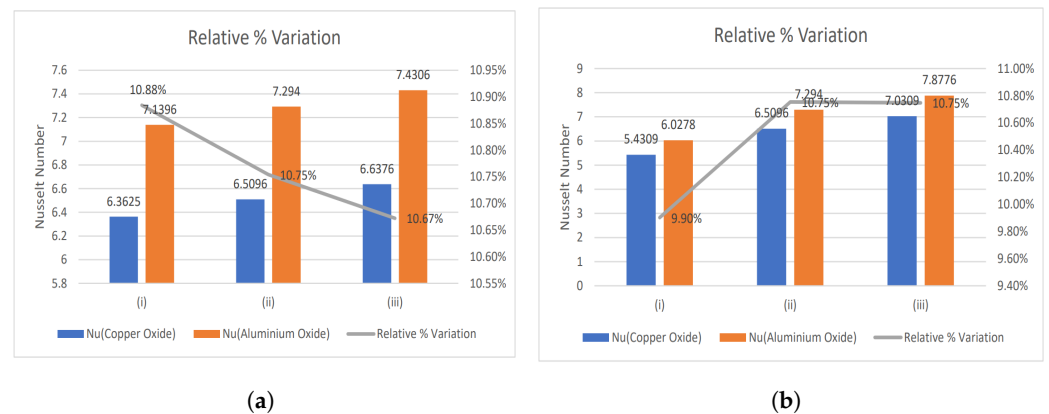


Figure 5. Relative % variation for (a) Casson fluid parameter (i) $\beta = 1$, (ii) $\beta = 2$, (iii) $\beta = 10$, and (b) Prandtl number (i) $Pr = 14$, (ii) $Pr = 21$, (iii) $Pr = 25$.

4.2. Influence of Nanoparticle Diameter and Volume Fraction

The impact of nanoparticle diameter and volume fraction for CuO and Al₂O₃-nanoparticles on temperature and Nusselt number is represented by Figures 6 and 7. There is a decrement in the temperature values with increasing volume fraction of CuO nanoparticles, whereas an increment is observed with the diameter of nanoparticles. In contrast, an opposite trend for Al₂O₃-nanoparticles is analyzed, i.e., temperature boosts with increment in nanoparticle volume fraction and shows declination with enhancement in the diameter of nanoparticles. Also, the Nusselt number depicts the same variation in both cases, as shown in Figure 7a,b.

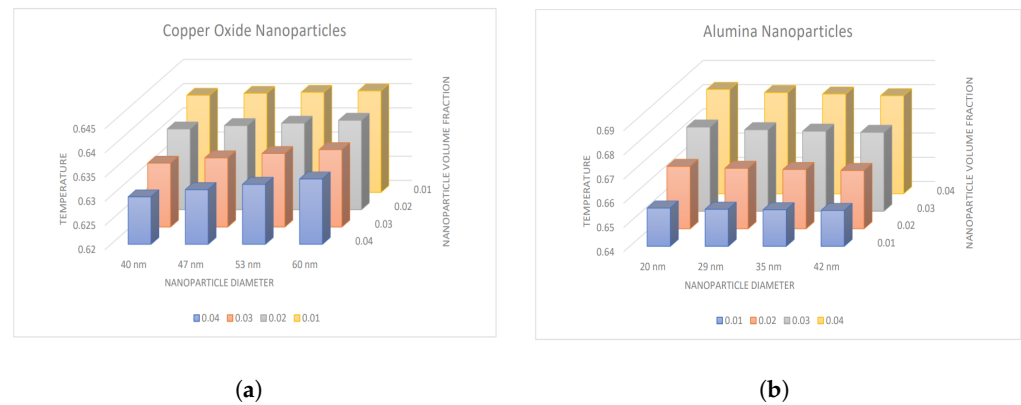


Figure 6. Variation in temperature with nanoparticle diameter and volume fraction for (a) CuO-nanoparticles, (b) Al₂O₃-nanoparticles.

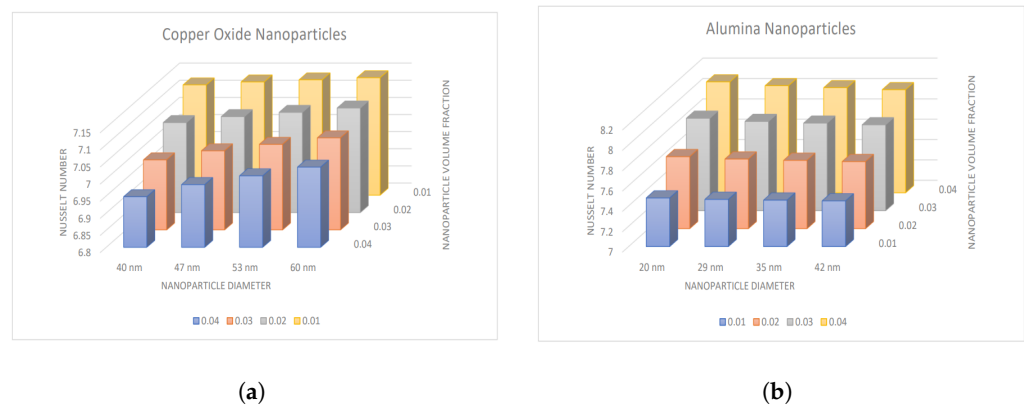


Figure 7. Variation in Nusselt number with nanoparticle diameter and volume fraction for (a) CuO-nanoparticles, (b) Al₂O₃-nanoparticles.

4.3. Velocity Contours

The velocity contours for wall slip velocity and nanoparticle volume fraction are illustrated by Figures 8–11. It is examined that the velocity rises as the w_s values rise. No-slip velocity is typically considered at the artery wall, which has the least importance. As a result, the boundary conditions in the current investigation have been used to introduce wall slip at the artery wall by assuming the walls to be permeable. The area for maximum velocity first reduces as the w_s value rises from $w_s = 0$ to $w_s = 0.05$, then expands as the value rises to $w_s = 0.1$. Figures 8 and 9 reveal that a similar behavior is noticed for both CuO and Al₂O₃ nanoparticles. The velocity shows declination with increasing volume fraction of both CuO and Al₂O₃ nanoparticles as depicted by Figures 10 and 11. In the case of CuO nanoparticles, the maximum velocity region grows as the nanoparticle volume fraction reaches its maximum value. Additionally, there are more trapped bolus. In contrast, for Al₂O₃ nanoparticles, the maximum velocity region first exhibits a drop and subsequently increases. Additionally, there are fewer trapped bolus.

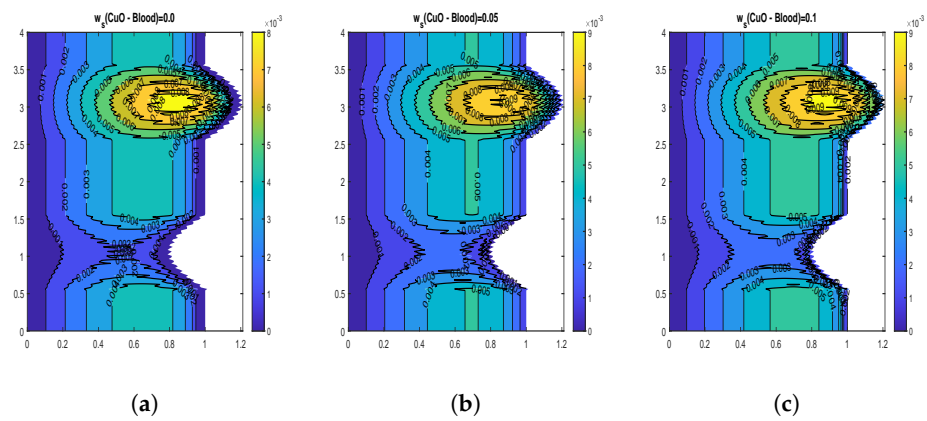


Figure 8. Blood flow patterns for wall slip velocity (a) $w_s = 0.0$, (b) $w_s = 0.05$, (c) $w_s = 0.1$ for CuO-Blood.

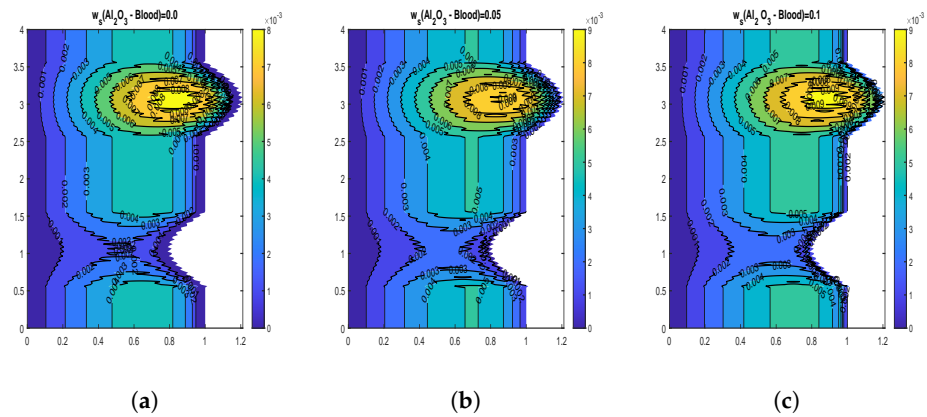


Figure 9. Blood flow patterns for wall slip velocity (a) $w_s = 0.0$, (b) $w_s = 0.05$, (c) $w_s = 0.1$ for Al_2O_3 -Blood.

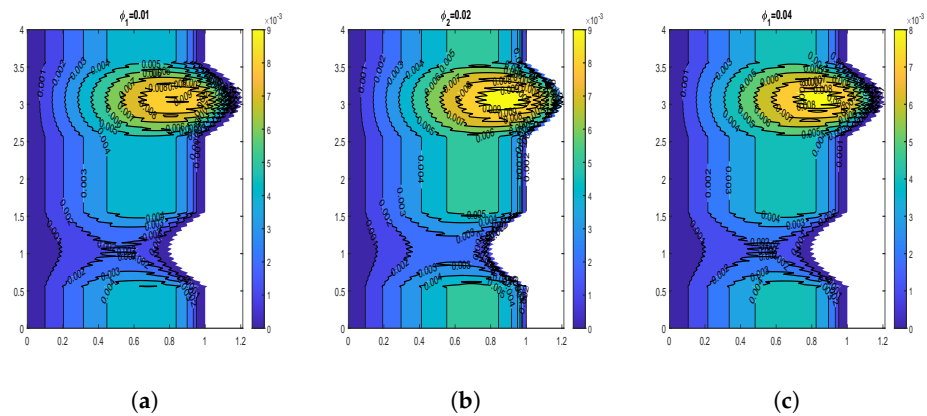


Figure 10. Blood flow patterns for volume fraction of CuO-nanoparticles (a) $\phi_1 = 0.01$, (b) $\phi_1 = 0.02$, (c) $\phi_1 = 0.04$.

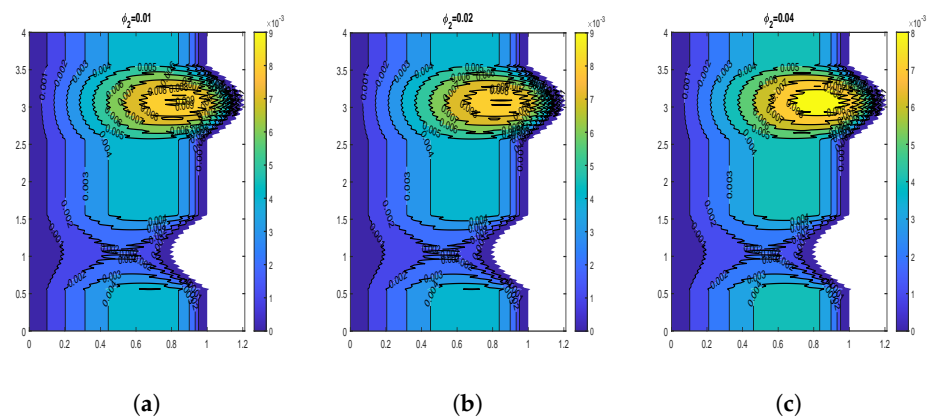


Figure 11. Blood flow patterns for volume fraction of Al_2O_3 -nanoparticles (a) $\phi_2 = 0.01$, (b) $\phi_2 = 0.02$, (c) $\phi_2 = 0.04$.

4.4. Impact of Electric Field Parameter

The velocity and temperature profiles for the electric field parameter are shown in Figures 12 and 13. With higher electric field parameter E_1^* , there is a rising tendency for flow velocities and temperature. The electric field adds an accelerating force in the direction of the applied electric field, which causes the thickness of the momentum boundary layer to increase and causes the fluid to accelerate. Increased fluid velocity also causes a rise in velocity gradients, which in turn causes an increase in viscous dissipations. Hence, an increment in the temperature profiles. Figure 14 represents wall shear stress profiles for different values of E_1^* . The profiles show an increasing trend with E_1^* . The flow rate and impedance profiles for E_1^* are depicted in Figures 15 and 16. The flow rate increases with an increase in E_1^* and, as expected, the opposite behavior for impedance profiles is observed.

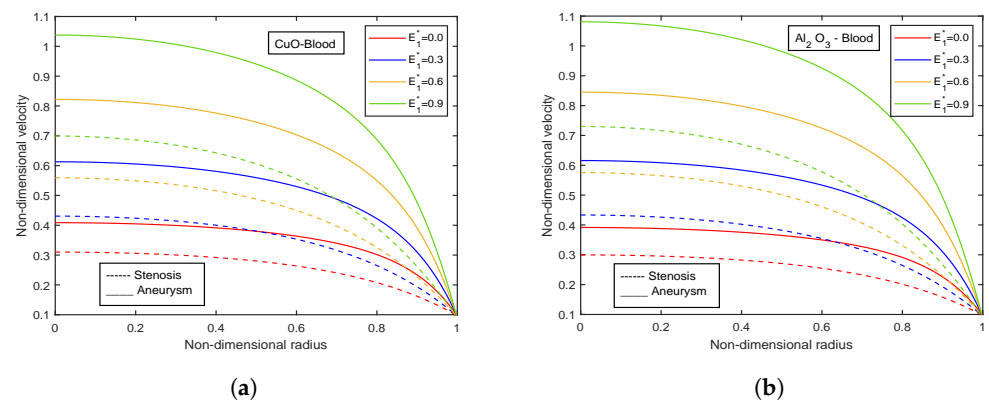


Figure 12. Velocity profiles of electric field parameter E_1^* for (a) CuO-nanoparticles, (b) Al_2O_3 -nanoparticles.

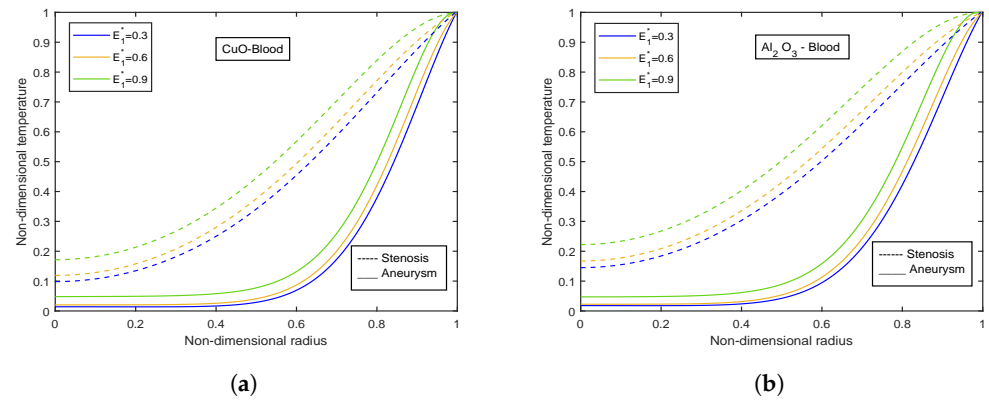


Figure 13. Temperature profiles of electric field parameter E_1^* for (a) CuO-nanoparticles, (b) Al₂O₃-nanoparticles.

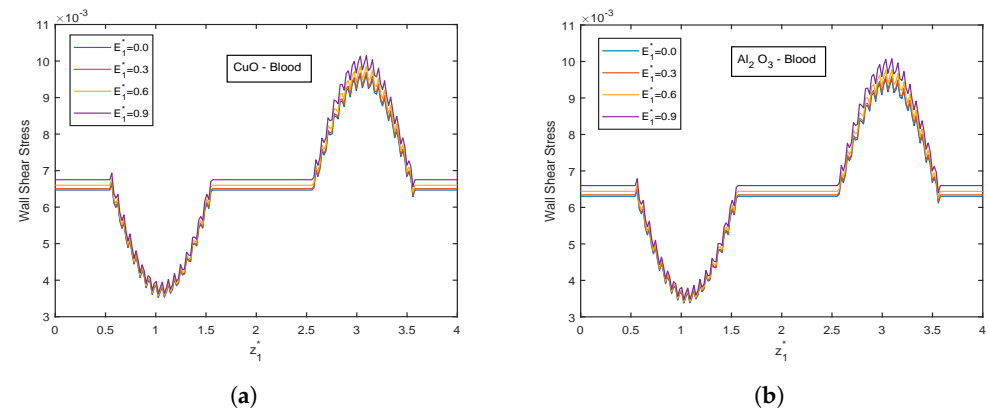


Figure 14. Wall shear stress profiles of electric field parameter E_1^* for (a) CuO-nanoparticles, (b) Al₂O₃-nanoparticles at $t_1^* = 1.2$.

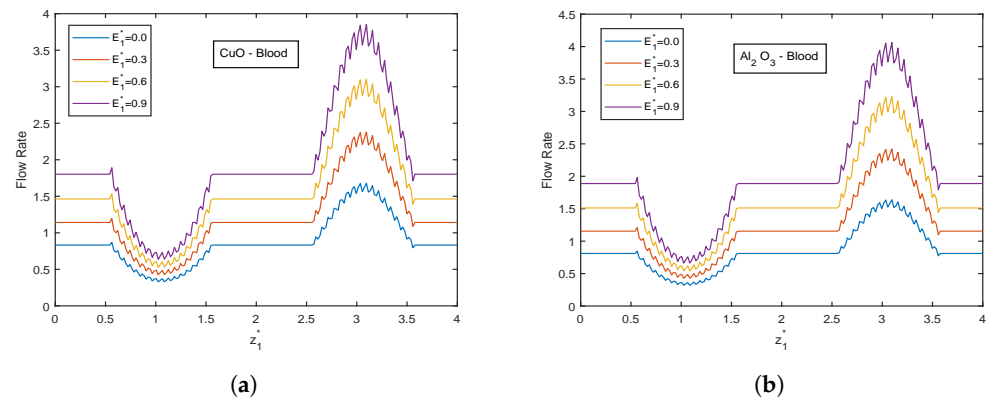


Figure 15. Flow rate profiles of electric field parameter E_1^* for (a) CuO-nanoparticles, (b) Al₂O₃-nanoparticles at $t_1^* = 1.2$.

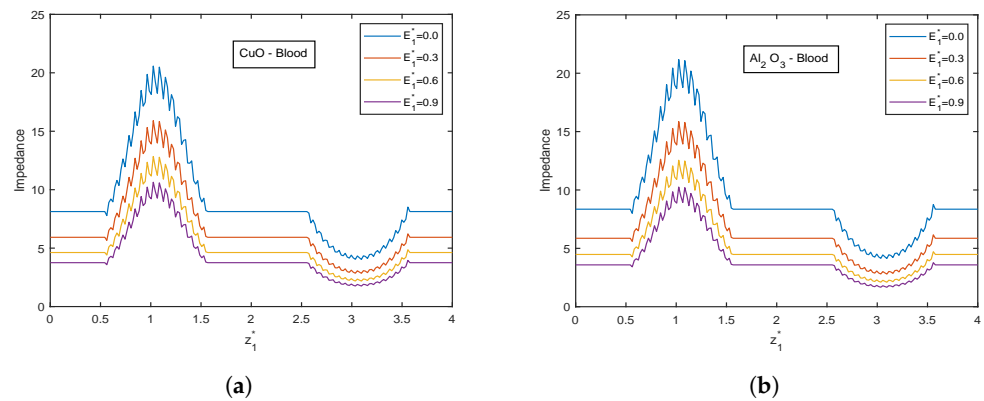


Figure 16. Impedance profiles of electric field parameter E_1^* for (a) CuO-nanoparticles, (b) Al₂O₃-nanoparticles at $t_1^* = 1.2$.

4.5. Effect of Viscosity Parameter

The influence of viscosity parameter β_0 is highlighted in Figures 17–21. The velocity profiles show inclination with increasing values of β_0 for both CuO and Al₂O₃ nanoparticles as conveyed by Figure 17a,b. This is because the resistance among the particles decreases when the magnitude of β_0 increases, indicating a rise in the velocity profiles. The temperature profiles show declination with enhancing β_0 values. An increment of 32.21% in the stenotic zone and 19.77% in the aneurysm zone is noticed when comparing the results for CuO and Al₂O₃ nanoparticles shown in Figure 18a,b. Figure 19 displays the profiles for wall shear stress for various β_0 values. As β_0 rises, the fluid becomes less viscous, enhancing the wall shear stress. Figures 20 and 21 display flow rate and impedance profiles for various values of β_0 . In the case of nanofluids, the flow rate rises as the value of β_0 rise, showing a viscosity reduction and leading to faster blood flow. Greater β_0 values represent a reduction in viscosity, which lowers impedance values.

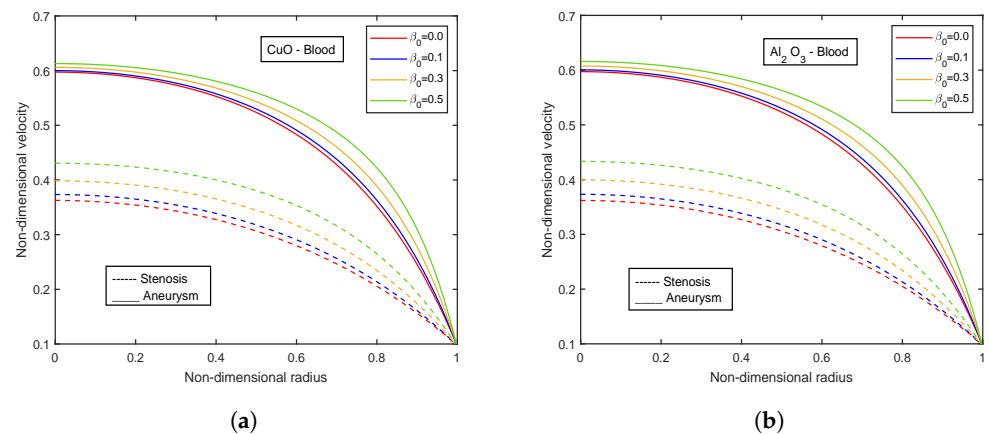


Figure 17. Impact of viscosity parameter β_0 on velocity profiles for (a) CuO-nanoparticles, (b) Al₂O₃-nanoparticles.

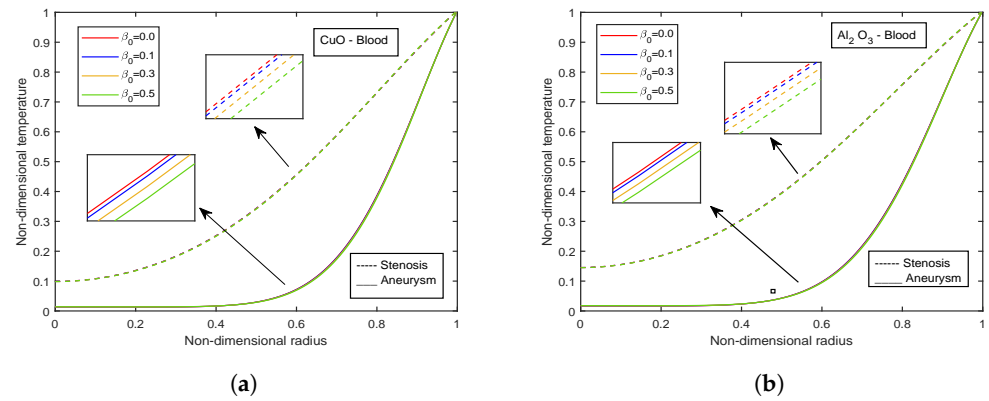


Figure 18. Impact of viscosity parameter β_0 on temperature profiles for (a) CuO-nanoparticles, (b) Al₂O₃-nanoparticles.

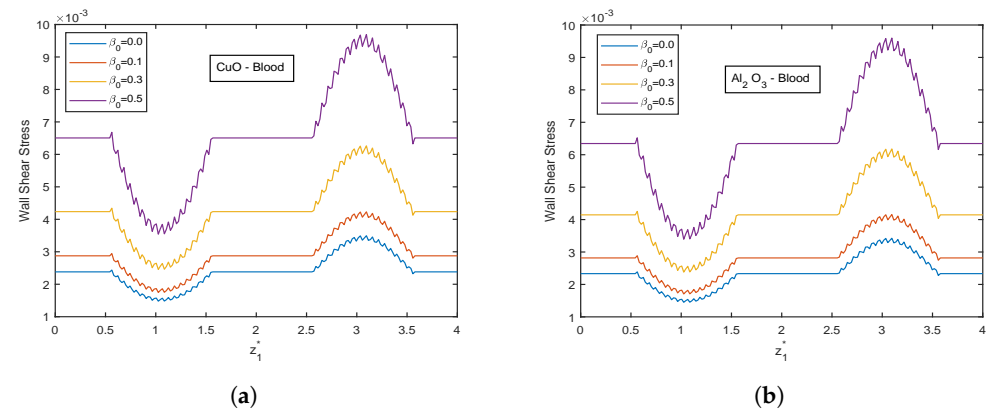


Figure 19. Wall shear stress profiles of viscosity parameter β_0 for (a) CuO-nanoparticles, (b) Al₂O₃-nanoparticles at $t_1^* = 1.2$.

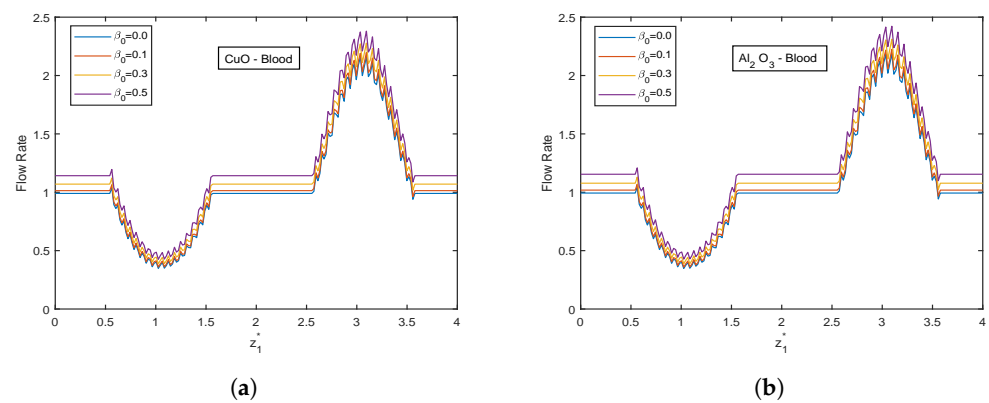


Figure 20. Flow rate profiles of viscosity parameter β_0 for (a) CuO-nanoparticles, (b) Al₂O₃-nanoparticles at $t_1^* = 1.2$.

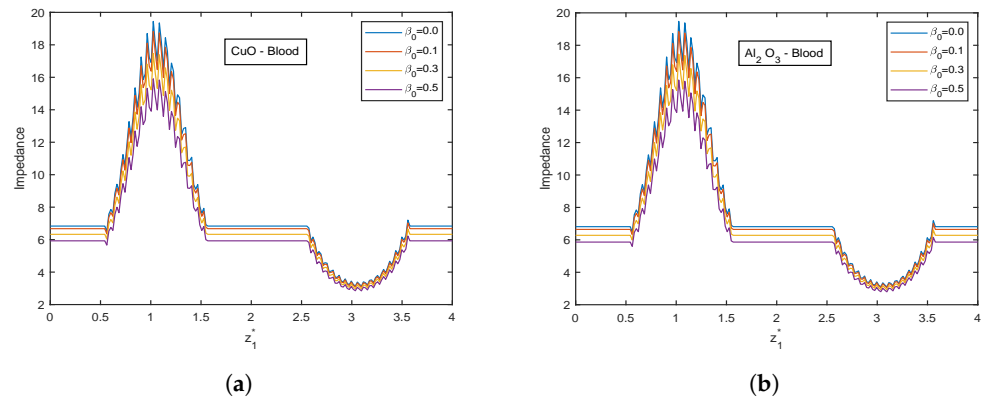


Figure 21. Impedance profiles of viscosity parameter β_0 for (a) CuO-nanoparticles, (b) Al_2O_3 -nanoparticles at $t_1^* = 1.2$.

4.6. Impact of Volume Fraction of Nanoparticles

Figures 22 and 23 depict the velocity and temperature profiles for different volume fractions of CuO-nanoparticles and Al_2O_3 -nanoparticles, respectively. A higher volume proportion of nanoparticles reduces the fluid velocity. These flows are hindered by the growing magnetic viscosity that is related to the velocity dampening. Both the nanoparticles show a decreasing trend for velocity. However, Al_2O_3 -nanoparticles observe slightly high-velocity values than CuO-nanoparticles of about 1.02% for the stenotic zone and 0.95% for the aneurysm region. Also, a comparison between stenotic and aneurysm regions reveals that velocity values in the aneurysm region are about 28.85% higher than that in the stenotic region. However, an opposite trend is observed for both the nanoparticle volume fractions in the case of temperature profiles. The temperature profiles decline with increasing volume fraction of CuO-nanoparticles, whereas an increment in temperature profiles is there with Al_2O_3 -nanoparticles volume fraction. Also, the temperature values for the stenotic zone are higher than that of the aneurysm region.

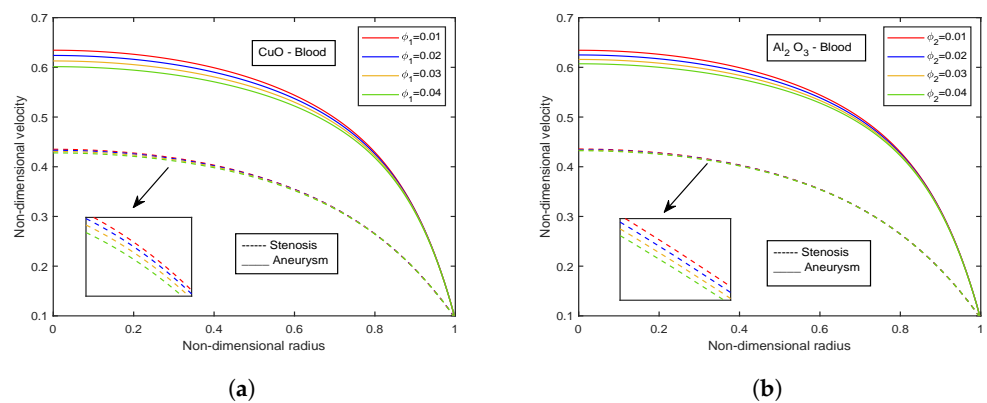


Figure 22. Influence of volume fraction of (a) CuO-nanoparticles, (b) Al_2O_3 -nanoparticles on velocity profiles.

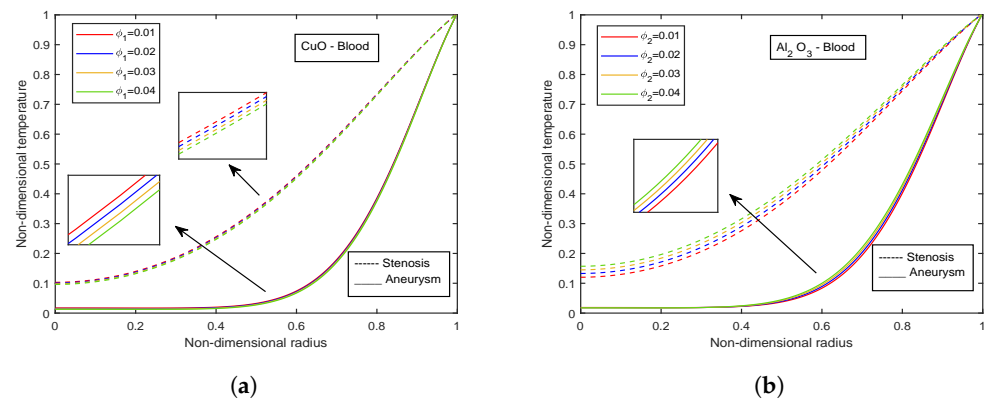


Figure 23. Influence of volume fraction of (a) CuO-nanoparticles, (b) Al₂O₃-nanoparticles on temperature profiles.

4.7. Effect of Casson Fluid Parameter

The influence of the Casson fluid parameter on the velocity and temperature profiles is depicted in Figures 24 and 25. The Casson parameter varies inversely with the yield stress and is associated with the non-Newtonian Casson fluid character. Therefore, boosting β lowers the fluid’s yield stress, relaxing the fluid and allowing it to move more quickly. The velocity in the stenotic region is less than that in the aneurysm zone. The temperature profiles show an enhancement with increasing values of β . The Al₂O₃ nanofluid profiles are higher in magnitude by 30.96% than that of CuO- nanofluid. The stenotic zone has a higher temperature than the aneurysm zone. The wall shear stress profiles increase with rising β values, as illustrated in Figure 26. In the stenotic zone, CuO-nanofluid shows an increase of 4.18% over Al₂O₃-nanofluid. The flow rate profiles for β are displayed in Figure 27. The flow rate profiles follow the same trend as wall shear stress profiles. The fluid flows more easily as β increases because the yield stress of the fluid is reduced. As a result, there is less resistance in the fluid’s pathway, and impedance profiles decline as β enhances (Figure 28).

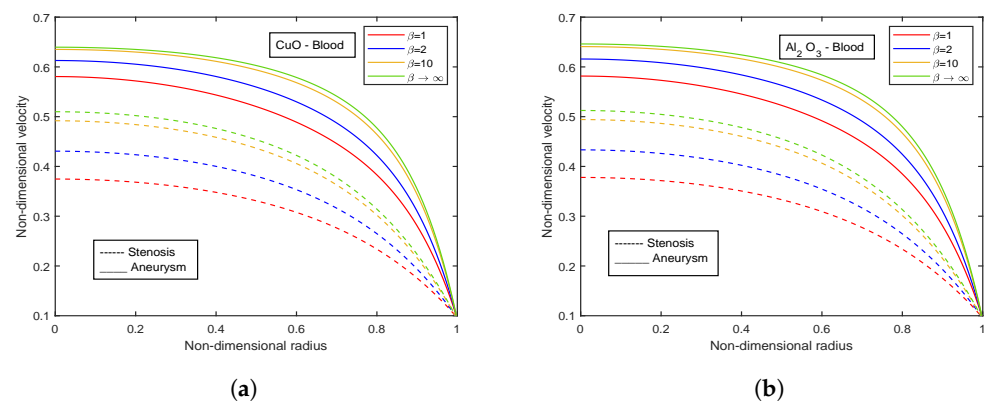


Figure 24. Velocity profiles of Casson fluid parameter β for (a) CuO-nanoparticles, (b) Al₂O₃-nanoparticles.

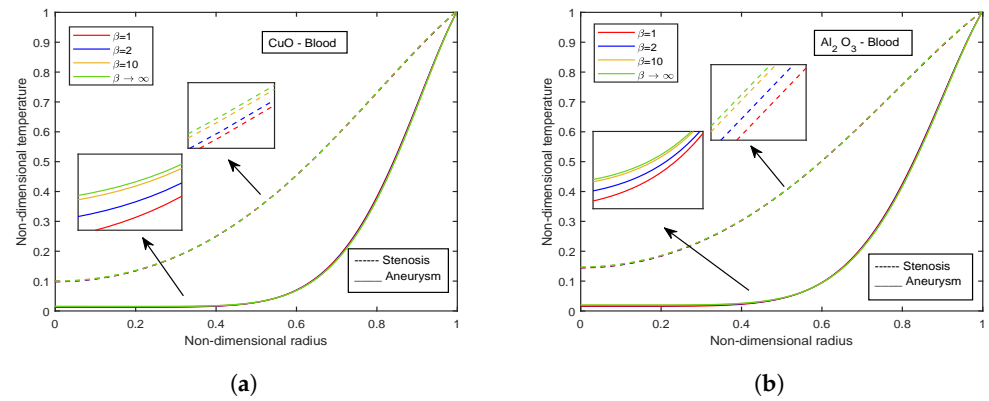


Figure 25. Temperature profiles of Casson fluid parameter β for (a) CuO-nanoparticles, (b) Al_2O_3 -nanoparticles.

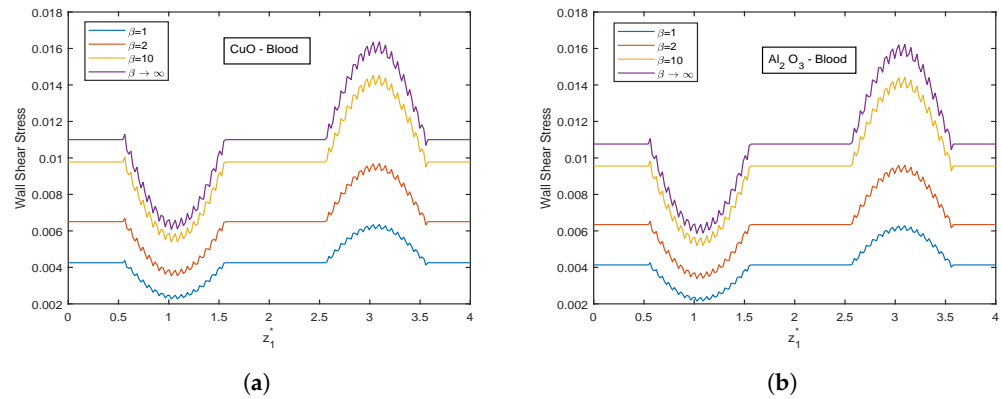


Figure 26. Wall shear stress profiles of Casson fluid parameter β for (a) CuO-nanoparticles, (b) Al_2O_3 -nanoparticles.

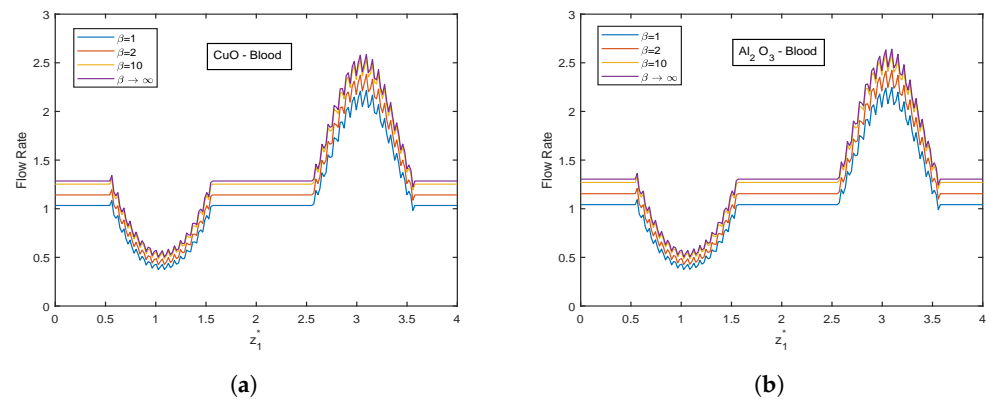


Figure 27. Flow rate profiles of Casson fluid parameter β for (a) CuO-nanoparticles, (b) Al_2O_3 -nanoparticles at $t_1^* = 1.2$.

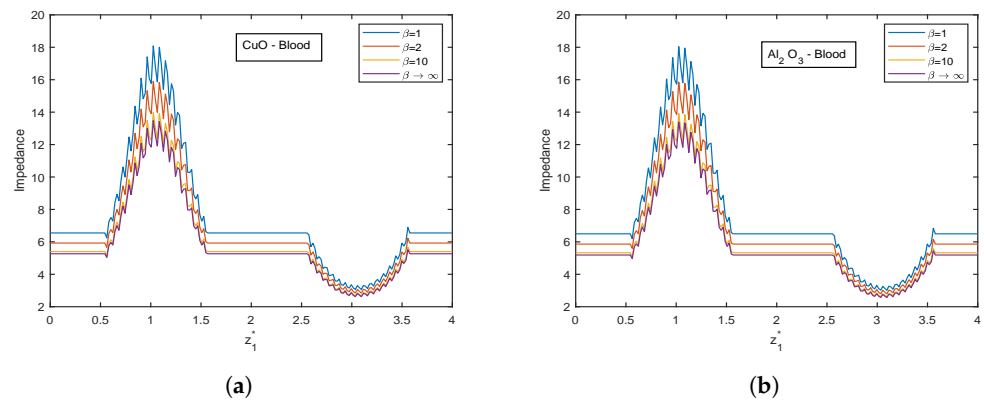


Figure 28. Impedance profiles of Casson fluid parameter β for (a) CuO-nanoparticles, (b) Al_2O_3 -nanoparticles at $t_1^* = 1.2$.

4.8. Effect of Radiation Parameter

The temperature profiles of radiation parameter Nr for CuO and Al_2O_3 nanoparticles are displayed in Figure 29a,b. The system seems to radiate the most heat because Nr affects thermal conductivity in the opposite manner. Radiation acts as a heat source within the bloodstream, and a spike in radiation exposure causes body temperature to rise. Free electrons in nanoparticles oscillate when right-wavelength light interacts with them. These oscillations produce heat that spreads across the surrounding area and kills cancerous cells. The use of this discovery in thermal therapy is extensive. The temperature values are higher in the stenotic region than in the aneurysm region. Comparing the temperatures for CuO and Al_2O_3 nanoparticles reported an improvement of 13.28% in the stenotic zone and 24.85% in the aneurysm region.

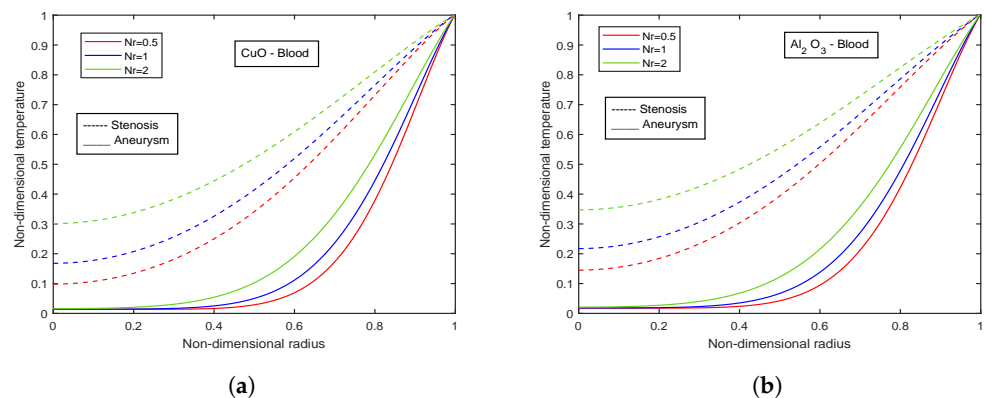


Figure 29. Influence of radiation parameter Nr on temperature profiles for (a) CuO-nanoparticles, (b) Al_2O_3 -nanoparticles.

4.9. Impact of Eckert Number

The temperature profiles for distinct values of Eckert number for CuO - Blood nanofluid and Al_2O_3 -Blood nanofluid are illustrated in Figure 30a,b. The temperature profiles rise with increasing values of Ec . Additionally, compared to Al_2O_3 -Blood nanofluid, CuO-Blood nanofluid has 30.6% greater magnitudes. The Eckert number connects the kinetic energy and enthalpy of a fluid. It's a term to describe how a fluid is affected when it self-heats due to dissipation effects. The temperature profiles are affected by temperature gradients at high flow velocities and by dissipation effects resulting from internal friction between the fluid layers. Self-heating causes temperature profiles to rise, and these effects, in turn, impact the temperature profiles.

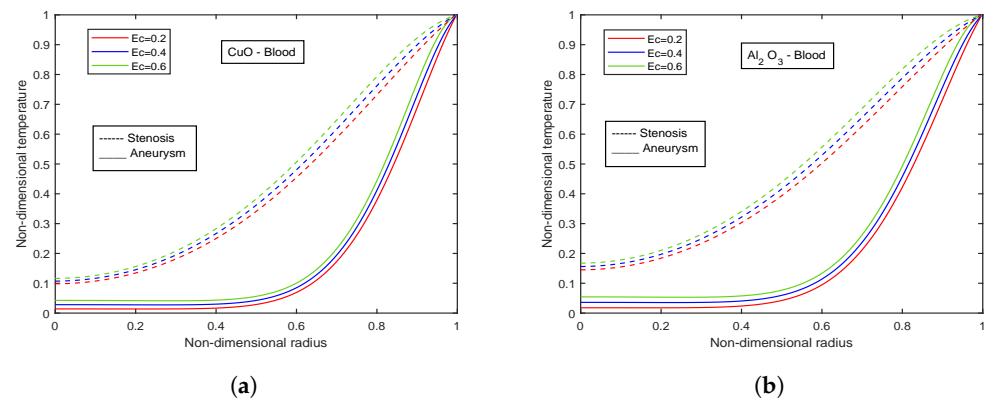


Figure 30. Temperature profiles of Eckert number Ec for (a) CuO-nanoparticles, (b) Al₂O₃-nanoparticles.

4.10. Effect of Prandtl Number

Figure 31a,b show the temperature profiles for different values of Prandtl number for CuO-Blood nanofluid and Al₂O₃-Blood nanofluid, respectively. An increase in Pr values accompanies the declination of the temperature profiles. The fluid’s viscosity and thermal diffusivity determine Pr. This dimensionless quantity links the momentum transport and the heat transport. The Prandtl number indicates whether heat is distributed more quickly in a fluid by convection or conduction. The Prandtl number has physical significance because, when it is less than 1, conductive heat transfer plays a significant role, transferring a higher percentage of heat than convection. Convective heat transfer takes precedence over conduction when the Prandtl value is higher than 1. A comparison between CuO-Blood nanofluid and Al₂O₃-Blood nanofluid reveals that Al₂O₃-Blood nanofluid reaches higher magnitudes for temperature by 23.94%. Also, the temperature values in the stenotic region are higher than in the aneurysm region.

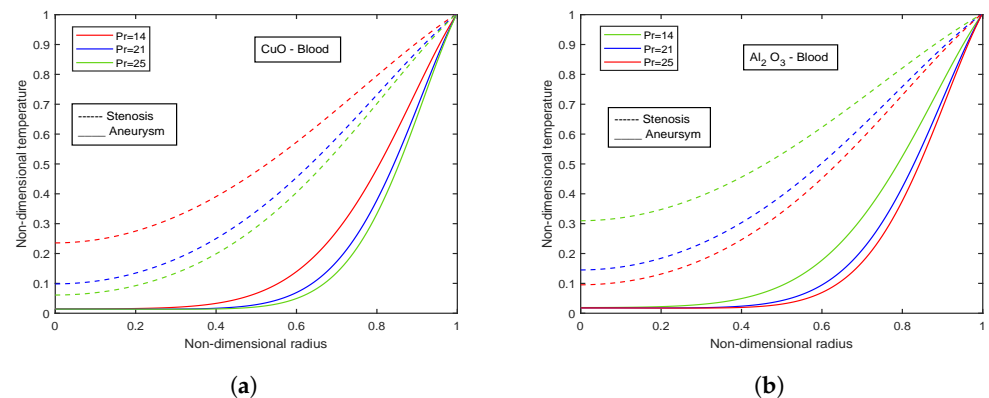


Figure 31. Impact of Prandtl number Pr on temperature profiles for (a) CuO-nanoparticles, (b) Al₂O₃-nanoparticles.

5. Conclusions

The present model aims to simulate blood flow through a permeable stenosed artery with an aneurysm subject to the combined effect of electric and magnetic field (EMHD) using two types of nanoparticles, namely CuO and Al₂O₃ considering blood as Casson fluid. The viscosity and thermal conductivity have been modeled using KKL correlations. The effect of Joule heating, radiation, and viscous dissipation is considered. The governing equations have been solved using the Crank-Nicolson scheme. The findings have been validated and are in good agreement with those in the literature. The relative % variation in the Nusselt number has been calculated. Some of the significant conclusions of the current study are listed below:

- The temperature and Nusselt number boost with enhancing diameter of CuO nanoparticles and decreasing diameter of Al₂O₃ nanoparticles.
- Velocity and temperature profiles show inclination with increasing electric field parameter E_1^* .
- There is an escalation in velocity and wall shear stress profiles with viscosity parameter β_0 .
- Flow rate ascends with increment in Casson fluid parameter β .
- Velocity descends with rising volume fraction of both CuO and Al₂O₃ nanoparticles.
- Temperature profiles elevate with volume fraction of Al₂O₃ nanoparticles, whereas declination is observed for CuO nanoparticles volume fraction.
- With increasing magnetic number, the relative % variation in the Nusselt number rises, but a decreasing trend is analyzed for the electric field parameter.

The application of nanotechnology in biomedicine is a fast-expanding subject with tremendous promises for enhancing the diagnosis and treatment of human disease. The ability to combine pharmaceuticals into a functionalized nanoparticle represents a new beginning for the selective delivery of therapeutics to tissues or cells. The present study's findings may be helpful in the diagnosis of hemodynamic abnormalities and the fields of nano-hemodynamics, nano-pharmacology, drug delivery, tissue regeneration, wound healing, and blood purification systems.

Author Contributions: B.K.S.: conceptualization, drafting the manuscript, supervision, validation, review and editing. R.G.: conceptualization, drafting the manuscript, methodology, investigation, software handling, supervision, validation, review and editing. N.K.M.: methodology, investigation, software handling, analysis, interpretation of data. Q.M.A.-M.: analysis, interpretation of data, review and editing. All authors have read and agreed to the published version of the manuscript.

Funding: This research was funded by 'United Arab Emirates University, Al Ain, UAE' grant number 12S086 and The APC was funded by 12S086.

Institutional Review Board Statement: Not applicable.

Informed Consent Statement: Not applicable.

Data Availability Statement: Not applicable.

Acknowledgments: The authors would like to acknowledge and express their gratitude to the United Arab Emirates University, Al Ain, UAE for providing financial support with Grant No. 12S086.

Conflicts of Interest: The authors declare no conflict of interest.

Nomenclature

r_1^*	Radial direction
Ec	Eckert Number
z_1^*	Axial direction
Pr	Prandtl Number
t_1^*	Time
Nr	Radiation parameter
u_1^*	Velocity component in radial direction
Nu	Nusselt number
w_1^*	Velocity component in axial direction
Da	Darcy number
U_0	Reference velocity
Re	Reynold's Number
R	Radius of artery in stenotic/aneurysm region
Gr	Grashof Number
R_0	Radius of artery in non-stenotic region
Q_1	Flow Rate
g	Acceleration by virtue of gravity

Greek Letters

\tilde{T}^*	Temperature of the base fluid
δ	Stenotic depth/Aneurysm height
\tilde{T}_1^*	Reference temperature
$\tilde{\theta}$	Non-dimensional temperature
\tilde{T}_w^*	Temperature at the wall
ρ	Density
B_0	Uniform Magnetic Field
ϕ_1	Volume fraction of CuO NPs
\tilde{C}_p^*	Specific heat at constant pressure
ϕ_2	Volume fraction of Al ₂ O ₃ NPs
E_0	Uniform Electric field
β_0	Viscosity constant
k_f	Thermal conductivity
λ	Resistance Impedance
p_1^*	Pressure
μ_f	Blood's viscosity
w_s	Wall slip velocity
μ_0	Reference viscosity
B_1	Pressure gradient parameter
d	Location of stenosis/aneurysm
σ	Electrical conductivity
L_0	Length of stenosis/aneurysm
τ_w	Shear stress at the wall
L	Length of the artery
α	Slip parameter
k_1^*	Permeability of the medium
β	Casson fluid parameter
M^2	Magnetic Number
γ	Thermal expansion coefficient

References

1. Ponalagusamy, R. Blood flow through an artery with mild stenosis: A two-layered model, different shapes of stenoses and slip velocity at the wall. *J. Appl. Sci.* **2007**, *7*, 1071–1077. [[CrossRef](#)]
2. Shaw, S.; Gorla, R.S.R.; Murthy, P.; Ng, C.O. Pulsatile Casson fluid flow through a stenosed bifurcated artery. *Int. J. Fluid Mech. Res.* **2009**, *36*, 43–63. [[CrossRef](#)]
3. Layek, G.; Mukhopadhyay, S.; Gorla, R.S.R. Unsteady viscous flow with variable viscosity in a vascular tube with an overlapping constriction. *Int. J. Eng. Sci.* **2009**, *47*, 649–659. [[CrossRef](#)]
4. Riahi, D.N.; Roy, R.; Cavazos, S. On arterial blood flow in the presence of an overlapping stenosis. *Math. Comput. Model.* **2011**, *54*, 2999–3006. [[CrossRef](#)]
5. Shaw, S.; Pradhan, S.; Murthy, P. A FSI model on the Casson fluid flow through an elastic stenosed artery. *Int. J. Fluid Mech. Res.* **2012**, *39*, 521–534. [[CrossRef](#)]
6. Shit, G.; Majee, S. Pulsatile flow of blood and heat transfer with variable viscosity under magnetic and vibration environment. *J. Magn. Magn. Mater.* **2015**, *388*, 106–115. [[CrossRef](#)]
7. Zaman, A.; Ali, N.; Sajid, M. Numerical simulation of pulsatile flow of blood in a porous-saturated overlapping stenosed artery. *Math. Comput. Simul.* **2017**, *134*, 1–16. [[CrossRef](#)]
8. Abdelsalam, S.I.; Mekheimer, K.S.; Zaher, A. Alterations in blood stream by electroosmotic forces of hybrid nanofluid through diseased artery: Aneurysmal/stenosed segment. *Chin. J. Phys.* **2020**, *67*, 314–329. [[CrossRef](#)]
9. Zhang, X.; Wang, E.; Ma, L.; Shu, C.; Zheng, L. Analysis of hemodynamics and heat transfer of nanoparticle-injected atherosclerotic patient: Considering the drag force and slip between phases of different particle shapes and volume fractions. *Int. J. Therm. Sci.* **2021**, *159*, 106637. [[CrossRef](#)]
10. Poonam; Sharma, B.; Kumawat, C.; Vafai, K. Computational biomedical simulations of hybrid nanoparticles (Au-Al₂O₃/blood-mediated) transport in a stenosed and aneurysmal curved artery with heat and mass transfer: Hematocrit dependent viscosity approach. *Chem. Phys. Lett.* **2022**, *800*, 139666. [[CrossRef](#)]
11. Basha, H.T.; Rajagopal, K.; Ahammad, N.A.; Sathish, S.; Gunakala, S.R. Finite Difference Computation of Au-Cu/Magneto-Bio-Hybrid Nanofluid Flow in an Inclined Uneven Stenosis Artery. *Complexity* **2022**, 2022. [[CrossRef](#)]

12. Waqas, H.; Farooq, U.; Hassan, A.; Liu, D.; Noreen, S.; Makki, R.; Imran, M.; Ali, M.R. Numerical and Computational simulation of blood flow on hybrid nanofluid with heat transfer through a stenotic artery: Silver and gold nanoparticles. *Results Phys.* **2023**, *44*, 106152. [[CrossRef](#)]
13. Badfar, H.; Yekani Motlagh, S.; Sharifi, A. Numerical simulation of magnetic drug targeting to the stenosis vessel using Fe₃O₄ magnetic nanoparticles under the effect of magnetic field of wire. *Cardiovasc. Eng. Technol.* **2020**, *11*, 162–175. [[CrossRef](#)]
14. Varmazyar, M.; Habibi, M.; Amini, M.; Pordanjani, A.H.; Afrand, M.; Vahedi, S.M. Numerical simulation of magnetic nanoparticle-based drug delivery in presence of atherosclerotic plaques and under the effects of magnetic field. *Powder Technol.* **2020**, *366*, 164–174. [[CrossRef](#)]
15. Ramadan, S.F.; Mekheimer, K.S.; Bhatti, M.M.; Moawad, A. Phan-Thien-Tanner nanofluid flow with gold nanoparticles through a stenotic electrokinetic aorta: A study on the cancer treatment. *Heat Transf. Res.* **2021**, *52*, 87–99. [[CrossRef](#)]
16. Saeed, A.; Khan, N.; Gul, T.; Kumam, W.; Alghamdi, W.; Kumam, P. The flow of blood-based hybrid nanofluids with couple stresses by the convergent and divergent channel for the applications of drug delivery. *Molecules* **2021**, *26*, 6330. [[CrossRef](#)]
17. Sharma, B.; Gandhi, R.; Bhatti, M. Entropy analysis of thermally radiating MHD slip flow of hybrid nanoparticles (Au-Al₂O₃/Blood) through a tapered multi-stenosed artery. *Chem. Phys. Lett.* **2022**, *790*, 139348. [[CrossRef](#)]
18. Mekheimer, K.S.; Abo-Elkhair, R.; Abdelsalam, S.; Ali, K.K.; Moawad, A. Biomedical simulations of nanoparticles drug delivery to blood hemodynamics in diseased organs: Synovitis problem. *Int. Commun. Heat Mass Transf.* **2022**, *130*, 105756. [[CrossRef](#)]
19. Khanduri, U.; Sharma, B.K. Hall and ion slip effects on hybrid nanoparticles (Au-GO/blood) flow through a catheterized stenosed artery with thrombosis. *Proc. Inst. Mech. Eng. Part C J. Mech. Eng. Sci.* **2022**, 09544062221136710. [[CrossRef](#)]
20. Sharma, B.K.; Poonam; Chamkha, A.J. Effects of heat transfer, body acceleration and hybrid nanoparticles (Au-Al₂O₃) on MHD blood flow through a curved artery with stenosis and aneurysm using hematocrit-dependent viscosity. *Waves Random Complex Media* **2022**, 1–31. [[CrossRef](#)]
21. Dolui, S.; Bhaumik, B.; De, S. Combined effect of induced magnetic field and thermal radiation on ternary hybrid nanofluid flow through an inclined catheterized artery with multiple stenosis. *Chem. Phys. Lett.* **2023**, *811*, 140209. [[CrossRef](#)]
22. Karmakar, P.; Ali, A.; Das, S. Circulation of blood loaded with trihybrid nanoparticles via electro-osmotic pumping in an eccentric endoscopic arterial canal. *Int. Commun. Heat Mass Transf.* **2023**, *141*, 106593. [[CrossRef](#)]
23. Walawender, W.P.; Chen, T.Y.; Cala, D.F. An approximate Casson fluid model for tube flow of blood. *Biorheology* **1975**, *12*, 111–119. [[CrossRef](#)] [[PubMed](#)]
24. Chakravarty, S.; Mandal, P.K. Numerical simulation of Casson fluid flow through differently shaped arterial stenoses. *Z. Angew. Math. Phys.* **2014**, *65*, 767–782.
25. Debnath, S.; Saha, A.K.; Mazumder, B.; Roy, A.K. Transport of a reactive solute in a pulsatile non-Newtonian liquid flowing through an annular pipe. *J. Eng. Math.* **2019**, *116*, 1–22. [[CrossRef](#)]
26. Ali, A.; Farooq, H.; Abbas, Z.; Bukhari, Z.; Fatima, A. Impact of Lorentz force on the pulsatile flow of a non-Newtonian Casson fluid in a constricted channel using Darcy's law: A numerical study. *Sci. Rep.* **2020**, *10*, 10629. [[CrossRef](#)]
27. Das, P.; Sarifuddin.; Rana, J.; Mandal, P.K. Solute dispersion in transient Casson fluid flow through stenotic tube with exchange between phases. *Phys. Fluids* **2021**, *33*, 61907. [[CrossRef](#)]
28. Padma, R.; Tamil Selvi, R.; Ponalagusamy, R. Electromagnetic control of non-Newtonian fluid (blood) suspended with magnetic nanoparticles in the tapered constricted inclined tube. *Proc. AIP Conf. Proc.* **2021**, 2336, 20008.
29. Beavers, G.S.; Joseph, D.D. Boundary conditions at a naturally permeable wall. *J. Fluid Mech.* **1967**, *30*, 197–207. [[CrossRef](#)]
30. Mishra, S.; Siddiqui, S.; Medhavi, A. Blood flow through a composite stenosis in an artery with permeable wall. *Appl. Appl. Math. Int. J. (AAM)* **2011**, *6*, 5.
31. Ijaz, S.; Nadeem, S. Examination of nanoparticles as a drug carrier on blood flow through catheterized composite stenosed artery with permeable walls. *Comput. Methods Programs Biomed.* **2016**, *133*, 83–94. [[CrossRef](#)]
32. Akbar, N.S.; Tripathi, D.; Bég, O.A. Variable-viscosity thermal hemodynamic slip flow conveying nanoparticles through a permeable-walled composite stenosed artery. *Eur. Phys. J. Plus* **2017**, *132*, 1–11. [[CrossRef](#)]
33. Shahzadi, I.; Bilal, S. A significant role of permeability on blood flow for hybrid nanofluid through bifurcated stenosed artery: Drug delivery application. *Comput. Methods Programs Biomed.* **2020**, *187*, 105248. [[CrossRef](#)]
34. Gandhi, R.; Sharma, B.; Kumawat, C.; Bég, O.A. Modeling and analysis of magnetic hybrid nanoparticle (Au-Al₂O₃/blood) based drug delivery through a bell-shaped occluded artery with joule heating, viscous dissipation and variable viscosity effects. *Proc. Inst. Mech. Eng. Part E J. Process Mech. Eng.* **2022**, *236*, 09544089221080273. [[CrossRef](#)]
35. Sharma, B.; Kumawat, C.; Makinde, O. Hemodynamical analysis of MHD two phase blood flow through a curved permeable artery having variable viscosity with heat and mass transfer. *Biomech. Model. Mechanobiol.* **2022**, 1–29. [[CrossRef](#)]
36. Kumawat, C.; Sharma, B.; Al-Mdallal, Q.M.; Rahimi-Gorji, M. Entropy generation for MHD two phase blood flow through a curved permeable artery having variable viscosity with heat and mass transfer. *Int. Commun. Heat Mass Transf.* **2022**, *133*, 105954. [[CrossRef](#)]
37. Sharma, B.; Gandhi, R. Combined effects of Joule heating and non-uniform heat source/sink on unsteady MHD mixed convective flow over a vertical stretching surface embedded in a Darcy-Forchheimer porous medium. *Propuls. Power Res.* **2022**, *11*, 276–292. [[CrossRef](#)]
38. Koo, J.; Kleinstreuer, C. Viscous dissipation effects in microtubes and microchannels. *Int. J. Heat Mass Transf.* **2004**, *47*, 3159–3169. [[CrossRef](#)]

39. Koo, J. *Computational Nanofluid Flow and Heat Transfer Analyses Applied to Micro-Systems*; North Carolina State University: Raleigh, NC, USA, 2005.
40. Li, J. *Computational Analysis of Nanofluid Flow in Microchannels with Applications to Micro-Heat Sinks and Bio-MEMS*. Ph.D. Thesis, Graduate Faculty of North Carolina State University, Raleigh, NC, USA, 2008.
41. Kandelousi, M.S. KKL correlation for simulation of nanofluid flow and heat transfer in a permeable channel. *Phys. Lett. A* **2014**, *378*, 3331–3339. [[CrossRef](#)]
42. Mehmood, K.; Hussain, S.; Sagheer, M. Numerical simulation of MHD mixed convection in alumina–water nanofluid filled square porous cavity using KKL model: Effects of non-linear thermal radiation and inclined magnetic field. *J. Mol. Liq.* **2017**, *238*, 485–498. [[CrossRef](#)]
43. Rana, S.; Nawaz, M. Investigation of enhancement of heat transfer in Sutterby nanofluid using Koo–Kleinstreuer and Li (KKL) correlations and Cattaneo–Christov heat flux model. *Phys. Scr.* **2019**, *94*, 115213. [[CrossRef](#)]
44. Malik, Z.U.; Mallawi, F.O.; Haq, R.U. Thermal energy performance of nanofluid flow and heat transfer based upon KKL correlation in a rotating vertical channel with permeable surface. *Case Stud. Therm. Eng.* **2021**, *28*, 101447. [[CrossRef](#)]
45. Shahzad, F.; Bouslimi, J.; Gouadria, S.; Jamshed, W.; Eid, M.R.; Safdar, R.; Shamshuddin, M.; Nisar, K.S. Hydrogen energy storage optimization in solar-HVAC using Sutterby nanofluid via Koo–Kleinstreuer and Li (KKL) correlations model: A solar thermal application. *Int. J. Hydrogen Energy* **2022**, *47*, 18877–18891. [[CrossRef](#)]
46. Ramzan, M.; Shahmir, N.; Ghazwani, H.A.S.; Elmasry, Y.; Kadry, S. A numerical study of nanofluid flow over a curved surface with Cattaneo–Christov heat flux influenced by induced magnetic field. *Numer. Heat Transf. Part A Appl.* **2023**, *83*, 197–212. [[CrossRef](#)]
47. Ahmed, A.; Nadeem, S. Effects of magnetohydrodynamics and hybrid nanoparticles on a micropolar fluid with 6-types of stenosis. *Results Phys.* **2017**, *7*, 4130–4139. [[CrossRef](#)]
48. Gandhi, R.; Sharma, B.K.; Makinde, O.D. Entropy analysis for MHD blood flow of hybrid nanoparticles (Au–Al₂O₃/blood) of different shapes through an irregular stenosed permeable walled artery under periodic body acceleration: Hemodynamical applications. *ZAMM J. Appl. Math. Mech./Z. Angew. Math. Mech.* **2022**, e202100532. [[CrossRef](#)]
49. Koo, J.; Kleinstreuer, C. Laminar nanofluid flow in microheat-sinks. *Int. J. Heat Mass Transf.* **2005**, *48*, 2652–2661. [[CrossRef](#)]
50. Ellahi, R.; Raza, M.; Vafai, K. Series solutions of non-Newtonian nanofluids with Reynolds’ model and Vogel’s model by means of the homotopy analysis method. *Math. Comput. Model.* **2012**, *55*, 1876–1891. [[CrossRef](#)]
51. Selimefendigil, F.; Öztop, H.F. Modeling and optimization of MHD mixed convection in a lid-driven trapezoidal cavity filled with alumina–water nanofluid: Effects of electrical conductivity models. *Int. J. Mech. Sci.* **2018**, *136*, 264–278. [[CrossRef](#)]
52. Burton, A.C. *Physiology and Biophysics of the Circulation*. *Acad. Med.* **1965**, *40*, xxx–xxxvi.
53. Anderson, J.D.; Wendt, J. *Computational Fluid Dynamics*; Springer: Berlin/Heidelberg, Germany, 1995; Volume 206.
54. Zaman, A.; Ali, N.; Kousar, N. Nanoparticles (Cu, TiO₂, Al₂O₃) analysis on unsteady blood flow through an artery with a combination of stenosis and aneurysm. *Comput. Math. Appl.* **2018**, *76*, 2179–2191. [[CrossRef](#)]

Disclaimer/Publisher’s Note: The statements, opinions and data contained in all publications are solely those of the individual author(s) and contributor(s) and not of MDPI and/or the editor(s). MDPI and/or the editor(s) disclaim responsibility for any injury to people or property resulting from any ideas, methods, instructions or products referred to in the content.